KYOTO UNIVERSITY

DOCTORAL THESIS

Structure of the outflow from super-massive black-hole seeds and its impact on the cosmological scales

Author:
Ignacio BOTELLA LASAGA

Supervisor:
Dr. Shin MINESHIGE

A thesis submitted in fulfillment of the requirements for the degree of Doctor of Astrophysics

in the

Department or Astronomy

January 24, 2022

Declaration of Authorship

I, Ignacio BOTELLA LASAGA, declare that this thesis titled, "Structure of the outflow from super-massive black-hole seeds and its impact on the cosmological scales" and the work presented in it are my own. I confirm that:

- This work was done wholly while in candidature for a research degree at this University.
- Where I have consulted the published work of others, this is always clearly attributed.
- Where I have quoted from the work of others, the source is always given. With the exception of such quotations, this thesis is entirely my own work.
- I have acknowledged all main sources of help.
- Where the thesis is based on work done by myself jointly with others, I have made clear exactly what was done by others and what I have contributed myself.

Signed: Ignacio Botella Lasaga

Date: 07/01/2022

"People who believe they are ignorant of nothing have neither looked for, nor stumbled upon, the boundary between what is known and unknown in the universe."

Neil deGrasse Tyson

KYOTO UNIVERSITY

Abstract

Faculty of Science
Department or Astronomy

Doctor of Astrophysics

Structure of the outflow from super-massive black-hole seeds and its impact on the cosmological scales

by Ignacio BOTELLA LASAGA

It is one of the biggest issues in black hole (BH) astrophysics how to precisely evaluate BH feedback to its environments. Previous work attempting to evaluate these phenomena have been limited by lack of observation evidence, computational power or other constrains. Aiming at studying the unique gas dynamics of super-Eddington flow around supermassive black hole (SMBH) seeds at high redshift, we carried out axisymmetric two dimensional radiation hydrodynamic simulations through our Nested Simulation-Box (NSB) method. This novel method consists on dividing the simulation box into individual simulation boxes each covering around 3 orders of magnitude. This allows our NSB method to create a chain of simulations capable of covering any region of space between the cosmological inner boundary and the black hole boundary. For the cases we study in this thesis we used 2 distinct simulation boxes, the first covering the inner zone at $(2-3\times10^3)r_{\rm Sch}$ (with $r_{\rm Sch}$ being the Schwarzschild radius) and second covering the outer zone at $(2\times10^3-3\times10^6)r_{\rm Sch}$.

In order for these 2 boxes to form a single larger simulation we need to create a smooth connection between them. We perform such information exchange through several overlapping radii between both boxes. By first performing the first stage simulation, we can obtain the values for the physical quantities such as gas density, velocity, and radiation energy density, at the outer edge of the inner zone. Then we imprint this information onto the shared area of the outer zone in the 2^{nd} stage. This guarantees a smooth connection of the physical quantities and thus a continuation between the inner and outer zones. We can hence simulate the evolution of gas outflow over a wide spatial range from the BH scale, $r_{\rm in}=2r_{\rm Sch}$, to the cosmological simulation scale, $r_{\rm out}=3.0\times10^6 r_{\rm Sch}$ ($=3\times10^{-4}$ pc for a BH mass of $10^3M_\odot$). The use of a 3^{rd} stage is not necessary the cases studied in this work but it can be done following the same scheme. The reason behind this 2 stage limit is due to the variables becoming smooth over the 2^{nd} stage and thus extrapolation of their behaviour becomes trivial.

The detailed procedure of the NSB method is as follows: In the first stage we start the calculation by injecting mass through the outer boundary of the inner zone at a constant rate of $\dot{M}_{\rm inj}=10^3L_{\rm Edd}/c^2$, where $L_{\rm Edd}$ is the Eddington luminosity and c is the speed of light, with a small angular momentum ($r_{\rm Kep}\sim100r_{\rm Sch}$). At the center of the simulation box we place a candidate for SMBH seed (i.e., a Population III (PopIII) remnant) of mass $M_{\rm BH}=10^3M_\odot$. Powerful outflows are generated in the innermost region and they propagate from the inner zone to the outer zone. The outflows are characterized by velocity of $0.02c$ (or $0.7c$) and density of 10^{-17} (10^{-19}) g cm^{-3} for near the edge-on (face-on) direction.

Even in the outer zone the outflow is gradually accelerated as it travels by accepting radiation-pressure force. The final mass outflow rate at the outermost boundary is $\dot{M}_{\rm out} \sim 0.4 \times \dot{M}_{\rm inj}$. By extrapolating the outflow structure to a further larger scale, we find that the momentum and mechanical energy fluxes at $r \sim 0.1$ pc are $\sim 10 - 100 L_{\rm Edd}/c$ and $\sim 0.1 - 10 L_{\rm Edd}$, respectively. Moreover, we find that the impacts are highly anisotropic in the sense that larger impacts are given towards the face-on direction than in the edge-on direction. These results indicate that the BH feedback will more efficiently work on the interstellar medium than that assumed in the cosmological simulations.

In the second model studied in this work we reduced the injected mass ratio to $\dot{M}_{\rm inj} = 500 L_{\rm Edd}/c^2$, while keeping all the other initial conditions equal (i.e., low angular momentum, PopIII remnant). For this reduced injection model we find that the accretion process becomes more efficient raising the accreted percentage from $\sim 0.4 \dot{M}_{\rm inj}$ to $\sim 0.6 \dot{M}_{\rm inj}$. As a result of this efficient accretion process the subsequent generated wind is weaker, with velocity of $0.03c$ (or $0.7c$) and density of 10^{-18} (10^{-19}) g cm^{-3} for near the edge-on (face-on) direction. Doing the extrapolation to the cosmological inner boundary (i.e., 0.1 pc) we obtain in this case the momentum and mechanical energy fluxes values are $\sim 1 - 10 L_{\rm Edd}/c$ and $\sim 0.01 - 10 L_{\rm Edd}$. By adding the contribution of the radiation force to the energy flux we see the value around the edge-on direction rise, and we are left with a flux $\sim 0.1 - 10 L_{\rm Edd}$. This means that, for this model, the gas impact on the outer medium without the inclusion of radiation (i.e., gas momentum flux, and mechanical energy flux) is comparable to the ones assumed in cosmological simulations. However, when the radiation is accounted for, it shows that cosmological models underestimate the impact from the AGN feedback.

Acknowledgements

This project would not have been possible without the help of Prof. Shin Mineshige, whose advice and comments were always helpful and encouraging. Prof. Mineshige deepened my knowledge in the field of astrophysics and cosmology with our weekly meetings and talks. He also taught me how to better myself as a researcher, knowledge that I hope impart on my students when my time comes.

In addition, I am grateful to Prof. Ken Ohsuga, Tomohisa Kawashima, and Takaaki Kitaki whose patience and invaluable advice helped me in innumerable occasions. Thanks to them I learned about a side of numerical simulations unknown to me, and provided me with much needed aid when the program would not properly work.

I am deeply grateful to our department members. I was able to enjoy my Ph.D life and discuss about various researches with them: Keiichi Maeda, Takanori Sasaki, Shiu-Hang Lee, Norita Kawanaka, Yoshihiro Ueda, Tetsuya Nagata, Mikio Kurita, Kotaro Moriyama, Takumi Ogawa, Eishun Takeo, Haruoh Yasuda, Yuh Tsunetoe, Masayuki Furuno, Fumiya Maeda, Kohsuke Namekata, Ryoma Ouchi, Kazuma Wada, Yuya Ishizawa, Mutsuko Inoguchi, Saeko Oda, Chika Miyazawa, Yuta Nakagawa, Monica Imanishi, Yoshiki Toba, Shun Nagatomo, Satoshi Takeshige, Takashi Nagao, Syota Notsu, Yuta Notsu, Ryo Sawada, Tomoyasu Hayakawa, Mariko Kimura, Atsushi Tanimoto, Akihiro Yamanaka, Satoshi Yamada, Sanetaka Okada, Aki Machida, Satomi Tokuda, Yuzi Kotani, Tomoki Matsuoka, Shoji Ogawa, Kazuma Suzuki, Takaaki Seki, Ryosuke Kobashi, Kenta Setoguchi, Mei Maruo, Tomohiro Yoshitake, Ryosuke Uematsu, Kohki Uno, Haruyuki Okinaka, Keiko Ohara, Takako Nishiyama, Miyuki Kawamoto, Ayako Nagaoka, Noriko Itoh, Eri Okamoto, Yukiko Nakanisi and Shogo Yoshioka.

I would like to thank the Ministry of Education, Culture, Sports, Science and Technology of Japan for awarding me with the MEXT scholarship which made possible this project, and Cray XC50 at Center for Computational Astrophysics (CfCA), National Astronomical Observatory of Japan (NAOJ) which carried out my numerical simulations.

Finally, I want to thank Simon "Lowko" Heijnen for providing endless hours of entertainment that kept me sane and motivated thought the entire duration of the project.

Contents

List of Figures

List of Tables

List of Abbreviations

BH	**B**lack**H**ole
SMBH	**S**uper **M**assive **B**lack**H**ole
AGN	**A**ctive **G**alactic **N**ucleus
SDSS	**S**loan **D**igital **S**ky **S**urvey
MHD	**M**agneto**H**ydro**D**ynamics
GRMHD	**G**eneral **R**elativistic **M**agneto**H**ydro**D**ynamics
RHD	**R**adiation **H**ydro**D**ynamics
FLD	**F**lux-**L**imited **D**iffusion
NSB	**N**ested **S**imulation **B**ox

Physical Constants

Speed of Light	$c = 2.99792458 \times 10^{10}$ cm s^{-1}
Gravitational constant	$G = 6.67259 \times 10^{-12}$ cm^3 g^{-1} s^{-2}
Solar mass	$M_\odot = 1.989 \times 10^{33}$ g
Schwarzchild radius	$r_{\rm Sch} = 2.95 \times 10^5 \left(\frac{M}{M_\odot}\right)$ cm
Eddington luminosity	$L_{\rm Edd} = 1.26 \times 10^{38} \left(\frac{M}{M_\odot}\right)$ erg s^{-1}
Proton mass	$m_{\rm p} = 1.6726 \times 10^{-24}$ g
Electron mass	$m_{\rm e} = 9.1094 \times 10^{-28}$ g
Thomson cross-section	$\sigma_{\rm T} = 6.6524 \times 10^{-25}$ cm^2
Boltzmann constant	$k_{\rm B} = 1.3807 \times 10^{-16}$ cm^2 g s^{-2} K^{-1}
Stefan-Boltzmann constant	$\sigma_{\rm SB} = 5.670374 \times 10^{-5}$ erg cm^{-2} s^{-1} K^{-4}
Specific heat ratio	$\gamma = 5/3$
Radiation constant	$a_r = 7.5646 \times 10^{-15}$ erg cm^{-3} K^{-4}
Mean molecular weight	$\mu = 0.5$

List of Symbols

B	magnetic field	G
E	total energy	g cm^{-3}
e	internal energy	g cm^{-3}
$E_{\rm rad}$	radiation energy	g cm^{-3}
F	radiative flux	ergs s^{-1} cm^{-2}
J	current density	Bi cm^{-2}
M	mass	g
$\dot{M}$	mass flux	g s^{-1}
p	pressure	Ba
r	radius	cm
$r_{\rm Kep}$	Keplerian radius	$r_{\rm Sch}$
v	velocity	cm s^{-1}
z	redshift	
ϵ	radiative efficiency	
Φ	gravitational potential	erg g^{-1}
ρ	density	g cm^{-3}
$\Omega_{\rm K}$	Keplerian angular velocity	s^{-1}

Dedicated to...

I dedicate my dissertation work to my family and many friends. A special feeling of gratitude to my parents, Luis Botella and Olga Lasaga, whom provided me with exceptional role models to follow. Without their support I would never be where I am today. Also to my siblings, Alex, Maria and Inés for making me a better person.

I also dedicate this dissertation to my very dear friends, who have supported me throughout the process, and helped me be here today. I will always be thankful to Marc Barroso, Laura Moreno, Sergi Terrades, Francesc "Cesc" Cunillera and Josep Tous for all their help through the degree and master in Barcelona. To Jane Chang, Christian Párraga and Seongchun Yang, without their moral support I would have never finished this thesis.

I dedicate this work and give special thanks to my brothers in arms Ilia Sixtel and Jan Pack. They helped me make of Kyoto my new home, and they will always be family no matter where the future takes us.

Lastly I wanted to dedicate this work to a very special friend, Katarzyna Kasia Mizerska for being there for me throughout the entire doctorate program. You have been my best cheerleader and will always be my polish sister.

Chapter 1

Introduction

1.1 SMBHs at high-z

We will start this chapter by introducing the objects of study, i.e. supermassive black holes (SMBHs), and their associated problems. There are multiple observational studies conducted on SMBHs across the universe (e.g., Willott et al. 2010, Bañados et al. 2016, Jiang et al. 2016, Reed et al. 2017, Matsuoka et al. 2019, Yang et al. 2018, Wang et al. 2019). Of these objects there are some that present very large masses ($\sim 10^{9-10} M_{\odot}$) at a very early time ($z \sim 6-7$) (Fan et al. 2003, Bañados et al. 2018). These objects, which can be studied to a certain extend through observation (Paliya et al. 2019, Volonteri 2010, Natarajan 2011, Valiante et al. 2017, and Inayoshi, Visbal, and Haiman 2020), can not be satisfactorily answered through our current knowledge. But to understand better why do these particular SMBHs present a challenge to our current understanding of physics we need to first introduce what a SMBH is.

1.1.1 Definition of SMBHs

We define a supermassive black hole (SMBH or sometimes MBH) as the largest type of black hole (BH), with mass on the order of millions to billions of times the mass of the Sun ($M_{\odot}$). These SMBHs are thought to exist at the centre of most large galaxies, including the centre of our own galaxy, the Milky Way, although we only have confirmation of a handful of these objects (most are too far away to be observed).

For many years, astronomers had only indirect evidence for SMBHs, the most compelling of which was the existence of quasars in remote active galaxies. Observations of the energy output and variability timescales of quasars revealed that they radiate over a trillion times as much energy as our Sun from a region about the size of the Solar System. The only mechanism capable of producing such enormous amounts of energy is the conversion of gravitational energy into light by a MBH.

More recently, direct evidence for the existence of SMBHs has come from observations of material orbiting the centres of galaxies. The high orbital velocities of these stars and gas are easily explained if they are being accelerated by a massive object with a strong gravitational field that is contained within a small region of space – i.e. a supermassive black hole.

Through our knowledge of black hole evolution we understand the important role that SMBHs have on their embedded media. An example of this is the fact that the mass of the black hole is correlated with the stellar mass ($M_{\rm BH} - M_{\rm bulge}$ relation) and velocity dispersion ($M_{\rm BH} - \sigma$ relation) of the bulge of the galaxy. These discoveries over the past 20 years have led to the popular idea that black holes and galaxies co-evolve and that feedback of active galactic nuclei (AGN) during the growth phases of the black hole strongly affects the gas content and star formation in the host galaxy (Ho 2004; Kormendy and Ho 2013). Understanding the formation and

growth history of SMBHs, their influence on galaxy evolution, and the exotic phenomena of stellar dynamics and gas accretion in the SMBH environment has become a major theme in astronomy. How the SMBH feedback affects galaxy evolution remains a major unanswered question in astrophysics.

There are many unknowns on the study of the impact that SMBHs can make on their host environment. In recent simulations, while they demonstrated that it is possible to tune phenomenological AGN feedback prescriptions to produce massive galaxies that resemble the observed quiescent ellipticals (e.g., Pillepich et al. 2018, Habouzit et al. 2019, M. Tremmel et al. 2019), they could not obtain a satisfactory understanding of the actual physics of the AGN feedback. AGN jet powers are in principle sufficient to offset the cooling observed in X-rays in ellipticals and galaxy clusters (e.g., Mathews and Brighenti 2003, Gaspari, Ruszkowski, and Sharma 2012). On more recent work (i.e, Richard-Laferrière et al. 2020) they also found evidence of strong correlations between the radio mini-halos and the central AGN in clusters. Which means that AGN feedback may also play a fundamental role in re-energizing non-thermal particles in clusters.

However, this power is released in the very vicinity of the central SMBHs (on scales on the order of a gravitational radius, i.e., $\sim$ 20 AU for a billion solar mass BH, which is comparable to the size of the Solar System) and must be distributed over scales comparable to cooling radii, where the cooling time is comparable to the Hubble time ($\sim$ 100 kpc). Thus, one major challenge is to unravel how the energy released near the SMBH is distributed over nine orders of magnitude in distance (Ruszkowski et al. 2019).

The origin of SMBHs also remains an open field of research. Astrophysicists agree that black holes can grow by accretion of matter and by merging with other black holes. There are several hypotheses for the formation mechanisms and initial masses of the progenitors, or "seeds", of SMBH. Some examples are stellar black holes result from the collapse of massive stars or the collapse of massive clouds of gas during the early stages of the formation of the galaxy. Another idea is that a stellar black hole consumes enormous amounts of material over millions of years, growing to SMBH proportions. Yet another, is that a cluster of stellar black holes form and eventually merge into a SMBH. These potential formation paths for SMBHs were outlined in the Rees diagram Rees (1984) (see Figure 1.1).

Independently of the specific formation channel for the black hole seed, given sufficient mass nearby, it could accrete to become an intermediate-mass black hole and possibly a SMBH. That is, if the SMBH seed can keep this accretion process over a long period of time uninterrupted.

Once these SMBHs have been formed they will continue to grow and evolve. The majority of the mass growth of SMBHs is thought to occur through episodes of rapid gas accretion, which are observable as AGNs or quasars. Observations reveal that quasars were much more frequent when the Universe was younger, indicating that SMBH formed and grew early. A major constraining factor for theories of SMBH formation is the observation of distant luminous quasars, which indicate that SMBH of billions of solar masses had already formed when the Universe was less than one billion years old. This suggests that SMBH arose very early in the Universe, inside the first massive galaxies. Most astronomers agree that accretion of material onto the SMBH drives both AGN feedback and galactic jets making the study of these objects a key component for the understanding of the early universe.

But if SMBHs in general are poorly understood, the evolution and effects of these same object at high-z is even more problematic.

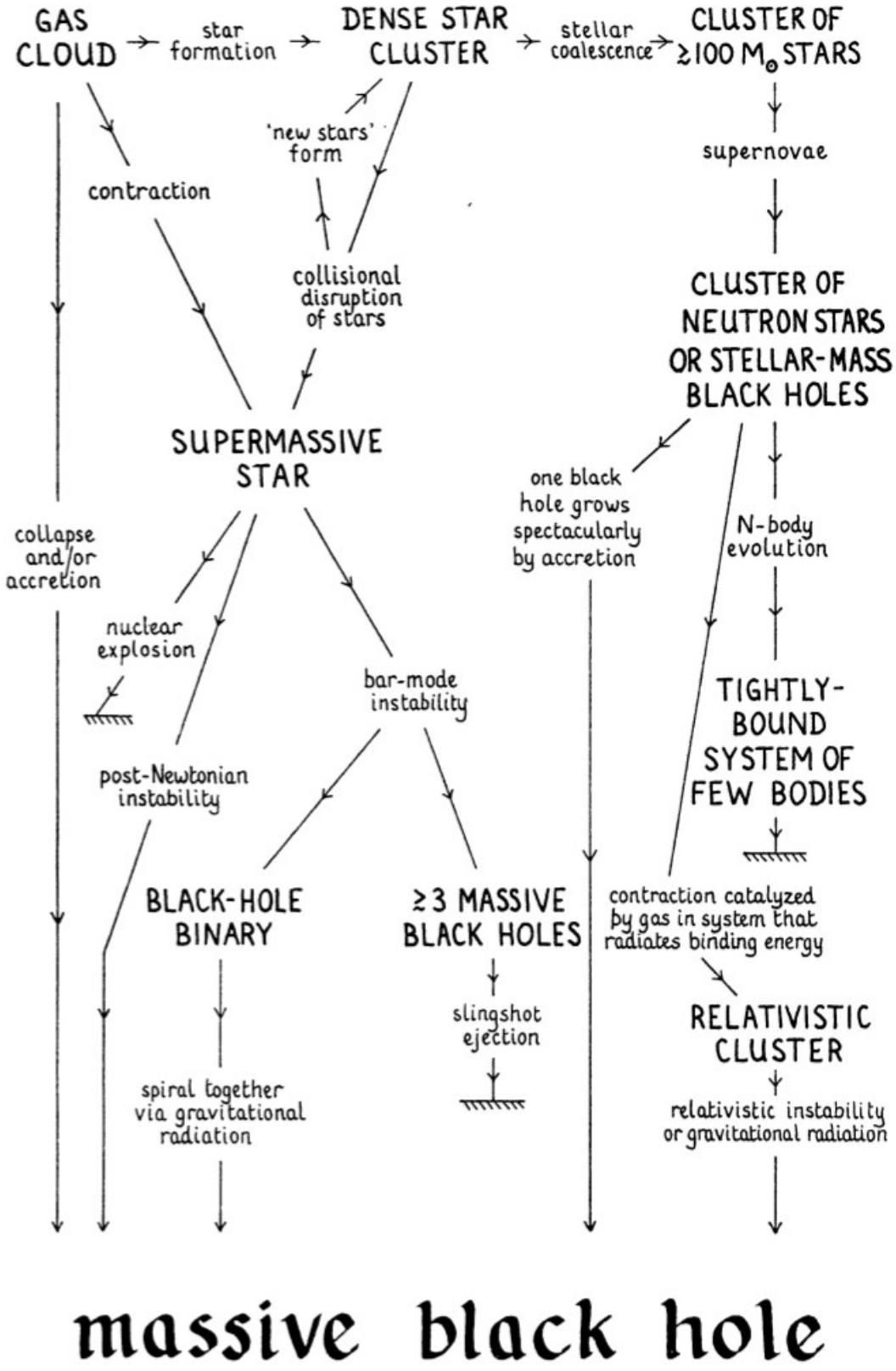

FIGURE 1.1: Original diagram from Rees (1978, 1984), outlining the possible formation pathways for supermassive black holes.

1.1.2 Problems of SMBHs at high-z

It is now generally accepted that most galaxies harbor SMBHs in their centres (Merloni and Heinz 2013; Graham 2016). This is true both for galaxies in the Local Universe and at high redshift, where almost 200 quasars have been discovered at $z > 6$ (Willott et al. 2010; Carnall et al. 2015; Matsuoka et al. 2016; Bañados et al. 2016; Jiang et al. 2016; Mazzucchelli et al. 2017; Reed et al. 2017; Wang et al. 2019; Matsuoka et al. 2018 a,b; Reed et al. 2019; Vito et al. 2019). These quasars are typically powered by SMBHs with masses of order $10^9 M_\odot$, yet are seen at lookback times > 13 Gyr, i.e. when the Universe was less than 800 Myr old (see Figure 1.2). The most extreme SMBH currently known is "Pōniuā'ena" with a mass of $M_{\rm Pon} = 1.5 \times 10^9 M_\odot$, seen at $z = 7.515$ (Yang et al. 2020), corresponding to $t = 700$ Myr after the Big Bang. These observations provide a rather tight constraint on the possible models of the origin and early growth of SMBHs.

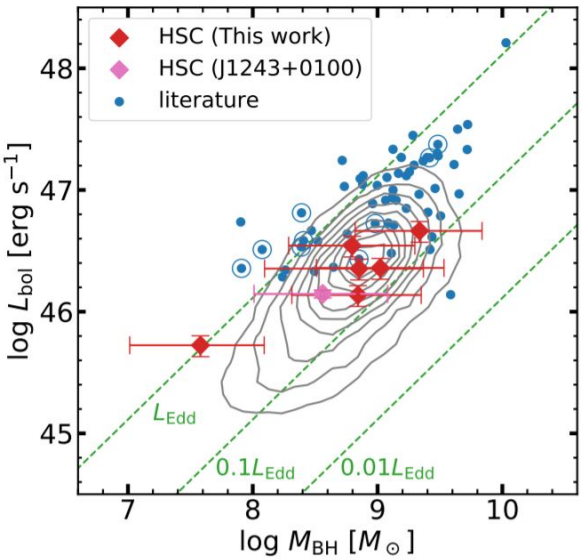

FIGURE 1.2: SMBH mass-luminosity plane of z > 5.8 quasars against the black hole mass $M_{\rm BH}$ measured to date with $\rm Mg_{II}$ (Onoue et al. 2019).

The mechanism by which such massive BHs formed within 1 Gyr after the big bang remains poorly understood. Generically, these SMBHs are thought to have assembled by mergers with other BHs and/or by gas accretion onto less massive BHs. If the first (seed) BHs are the $\sim 10^2 M_\odot$ remnant BHs of the first generation of stars (e.g., Heger et al. 2003), they must be in place well before redshift $z = 6$. If accretion onto BHs is limited at the Eddington rate with radiative efficiency ϵ, defined as the fraction of the rest-mass energy of matter falling onto the BH that is released as radiation, then $1 - \epsilon$ of the matter is accreted and the growth of the BH mass $M_{\rm BH}$ is given by

$$\frac{d \ln M_{\rm BH}}{dt} = \frac{1-\epsilon}{\epsilon} - \frac{4\pi G \mu m_p}{\sigma_{\rm T} c}, \tag{1.1}$$

where G is the gravitational constant, c is the speed of light, $\mu \approx 1.15$ is the mean atomic weight per electron for a primordial gas, and $\sigma_{\rm T}$ is the Thompson electron cross section. The e-folding timescale for mass growth is $t_{\rm Edd} \approx 4.4 \times 10^7$ yr for $\epsilon = 0.1$. In the concordance cosmological model, the time elapsed between redshifts

$z = 30$ (when the first seeds may form) and $z = 6.4$ (the redshift of the most distant quasar) is ≈ 0.77 Gyr, allowing for a mass growth by a factor of $\approx 10^{7.7}$. Therefore, individual $\sim 100 M_\odot$ seeds can grow into the SDSS detected quasar BHs through gas accretion alone, provided the accretion is uninterrupted at close to the Eddington rate and $\epsilon \leq 0.1$. A higher efficiency and/or a lower time-averaged accretion rate will require many seed BHs to merge together; the number of required mergers increases exponentially for lower time-averaged accretion rates.

In general, these models fall broadly into two groups (see Inayoshi, Visbal, and Haiman 2020, for a review). One group considers SMBHs growing from massive seeds: objects with masses $\sim 10^4 - 10^5 M_\odot$ (Ferrara et al. 2014) that form via direct gas collapse (Loeb and Rasio 1994; Begelman, Volonteri, and Rees 2006; Dijkstra, Ferrara, and Mesinger 2014; Chon et al. 2016; Wise et al. 2019), an intermediate supermassive star stage (Regan and Haehnelt 2009; Volonteri and Begelman 2010; Begelman 2010) or due to rapid mergers of stars and/or individual stellar-mass black holes in a dense cluster (Portegies Zwart and McMillan 2002; Portegies Zwart et al. 2004; Devecchi and Volonteri 2009). These seeds can then grow the required four orders of magnitude in mass over several hundred Myr even if the radiative efficiency of accretion is $\epsilon \gtrsim 0.1$.

The second kind of model suggests that SMBHs grow from stellar mass seeds (Madau and Rees 2001) via luminous accretion with a rather low radiative efficiency. Low efficiency may be achieved if accretion rates are hyper-Eddington; they create conditions where the photons emitted by the accreting gas cannot escape the accretion flow and are dragged into the black hole (Alexander and Natarajan 2014; Sądowski et al. 2015; Pacucci, Volonteri, and Ferrara 2015; Inayoshi, Haiman, and Ostriker 2016; Sakurai, Inayoshi, and Haiman 2016; Takeo, Inayoshi, and Mineshige 2020). Even if accretion consists of Eddington-limited thin disc episodes, a radiative efficiency $\epsilon \sim 0.06$ may be achieved if the spin of the black hole is kept low (e.g. King, Pringle, and Hofmann 2008). Since the black hole mass depends exponentially on $(1-\epsilon)/\epsilon$, this difference is enough to allow for the growth of SMBHs powering even the most extreme high-redshift quasars. The super-Eddington accretion flow theory is more supported since in the early Universe the conditions for this type of accretion onto BH (i.e, gas density and metallicity) are thought to have been favorable (Brightman et al. 2019).

Unfortunately, the limited data, and complexity of the studies, makes discerning the origin of these objects still a mystery. To understand to what degree the study of the origin of SMBH at high redshift is, we need to talk about the 3 different methods we have to "observe" these objects.

1.2 Studying SMBHs through observation

High redshift quasars, as the most luminous non-transient objects in the early universe (as shown in Figure 1.3), are the most promising tracers to address the history of cosmic reionization and how the origins of SMBHs are linked to galaxy formation and evolution. The huge amounts of energy released by the active SMBHs can have an impact on the life and evolution of their entire host galaxy. This has made AGNs relevant for an even broader community of astronomers. The study of AGNs in the context of their feedback effects has brought a number of unexpected discoveries (some of them described in this review) about the physical conditions of the gas in the surroundings of an active nucleus. Thus, the value of SMBH surveys, or to be more precise AGN feedback surveys, is vastly reaching. Its capability of opening a

window to study, not only the growth and evolution of the central object but also the conditions of the gas at certain times in the Universe is crucial.

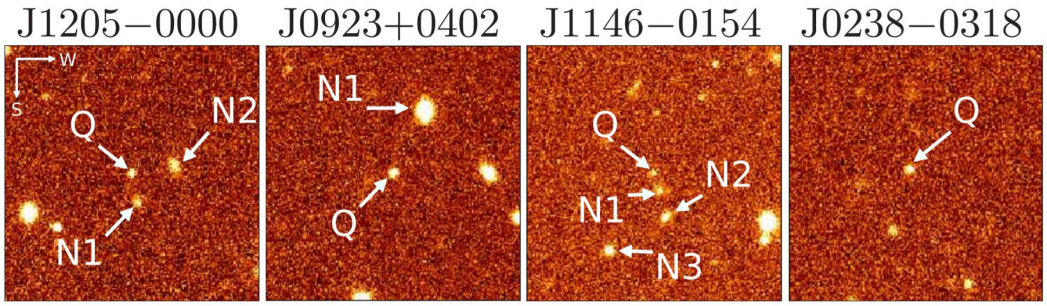

FIGURE 1.3: The HSC images of the red quasar candidates at $z > 5.6$. "Q" and "N" mark the quasar and nearby objects identified on the HSC. (Kato et al. 2020)

For decades, quasars have been detected and studied at increasingly high redshifts, owing to their extremely high luminosities. Wide-area surveys, required by the rarity of luminous, high-redshift quasars, provided an almost continuous progress of breaking redshift records. Since the first few $z \sim 6$ quasars were detected through (early) SDSS observations (e.g., Fan et al. 2003), the trickle has turned into a steady stream of detections. The current redshift record holder is the quasar ULAS J1342+0928 at $z = 7.54$ (Bañados et al. 2018a), and there are over 170 quasars known at $z \gtrsim 6$, in addition to over 300 at $z \sim 5 - 6$ (see King, Pringle, and Hofmann 2008). The vast majority of these systems have been selected in various wide-field, multi-band optical-IR surveys, through elaborate colour based criteria. Indeed, essentially every imaging survey with sufficient area and depth has identified samples of z & 5 quasars (for some of the largest relevant samples see, e.g., Willott et al. 2010a, Bañados et al. 2016, Jiang et al. 2016, Reed et al. 2017, Matsuoka et al. 2019, Yang et al. 2018, Wang et al. 2019a). The quasar selection criteria are constantly improving, allowing to recover highly complete (or, at least, well-understood) samples that cover an ever expanding range in flux, redshift, and/or colour (e.g., Carnall et al. 2015, Wang et al. 2016, Reed et al. 2017). The recent, publicly accessible compilation by Ross and Cross (2020) provides an impressive and up-to-date status report on this still-growing population of quasars, as well as references to some of the important follow-up observations. Most importantly, several teams have been accumulating a rich collection of multi-wavelength data for these systems, which allow to study a multitude of phenomena related to the quasars and their central engines, to their host galaxies, and indeed to their large-scale environments.

While capable of determining certain parameters of the AGN, observations of SMBHs can not study the conditions of the gas in a high-z scenario. Not only that but observation of these SMBHs can only be done through their hosts, the MeV blazars. These are the most luminous persistent sources in the Universe and emit most of their energy in the MeV band (Hopkins, Richards, and Hernquist 2007, Harrison et al. 2013). For these reasons the study of the accretion physics, the growth rate or the outflow structure on high-z SMBHs can not be obtained solely from observational data. That is, we need to introduce some tools, in addition, to fully understand the growth history of the SMBHs in the early Universe.

1.3 Studying SMBHs through cosmological simulations

The first one of these tools that we need to introduce are the cosmological simulations. Over the last decades, cosmological simulations of galaxy formation have been instrumental for advancing our understanding of structure and galaxy formation in the Universe. These simulations follow the nonlinear evolution of galaxies modeling a variety of physical processes over an enormous range of scales (Figure 1.4 gives us an idea of the range these studies cover). A better understanding of the physics relevant for shaping galaxies, improved numerical methods, and increased computing power have led to simulations that can reproduce a large number of observed galaxy properties. Modern simulations model dark matter, dark energy, and ordinary matter in an expanding space-time starting from well-defined initial conditions. The modeling of ordinary matter is most challenging due to the large array of physical processes affecting this matter component. Cosmological simulations have also proven useful to study alternative cosmological models and their impact on the galaxy population.

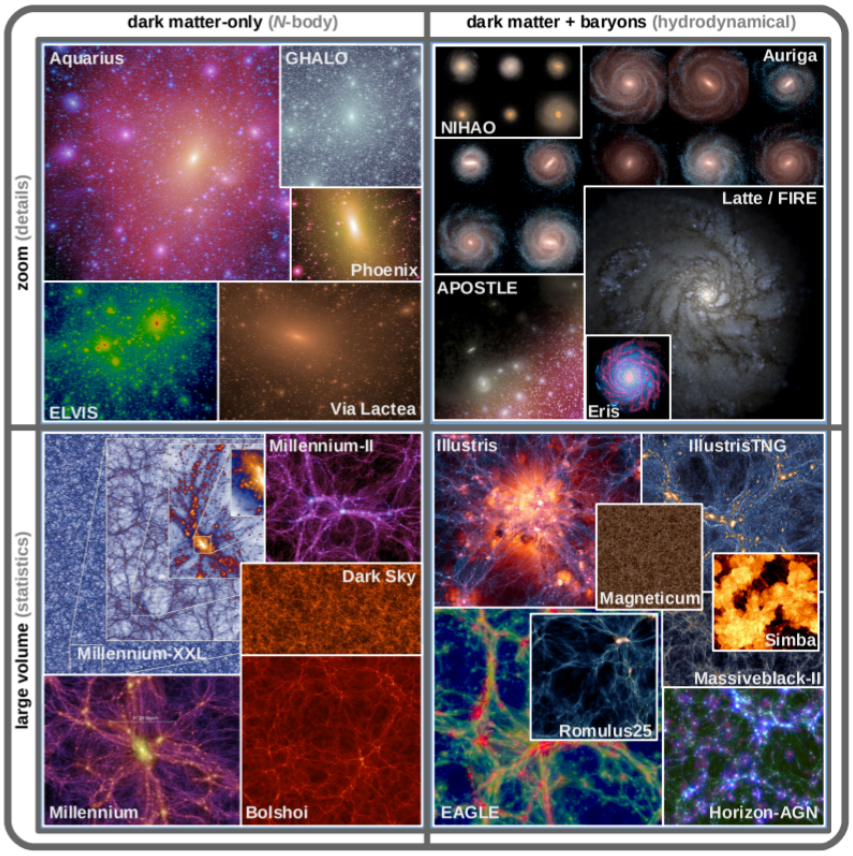

FIGURE 1.4: Visual representations of some selected recent structure and galaxy formation simulations. The simulations are divided in large volume simulations providing statistical samples of galaxies, and zoom simulations resolving smaller scales in more detail. Furthermore, they are also divided in dark matter-only, i.e. N-body, and dark matter plus baryons, i.e. hydrodynamical simulations (Vogelsberger et al. 2019).

Dark matter builds the backbone for the formation of galaxies, which are expected to form at the centers of dark matter overdensities, so-called halos. The continuum limit of non-interacting dark matter particles is described by the collisionless

Boltzmann equation (1.2) coupled to Poisson's equation (1.3). This pair of equations has to be solved in an expanding background Universe dictated by the Friedmann equations, which are derived from the field equations of general relativity.

$$\frac{df}{dt} = \frac{\partial f}{\partial t} + \mathbf{v}\frac{\partial f}{\partial r} - \frac{\partial \Phi}{\partial r}\frac{\partial f}{\partial \mathbf{v}} = 0, \tag{1.2}$$

$$\nabla^2 \Phi = 4\pi G \int f d\mathbf{v}, \tag{1.3}$$

where f is the distribution function of dark matter and Φ is the collective gravitational potential.

As explained in Vogelsberger et al. (2019), most cosmological simulations employ Newtonian rather than relativistic gravity, that provides a fairly good approximation since linear structure growth is identical in the matter dominated regime in the two theories, and non-linear large-scale structure induces velocities far below the speed of light. That is not to say that cosmological simulations dismiss completely relativistic factors such as the expansion effects of the Universe which they implement through the cosmic scaling factor, $a(t)$. Cosmological simulations are also typically performed with periodic boundary conditions to mimic the large-scale homogeneity and isotropy of the matter distribution of the Universe, i.e. the cosmological principle.

The N-Body method: N-body methods are often employed to follow the collisionless dynamics of dark matter, where the phase-space density is sampled by an ensemble of N phase-space points. N-body methods therefore solve the collisionless Boltzmann equation by the method of characteristics.

Simulating baryons is therefore crucial to make predictions for the visible Universe. Initially, the baryon component is solely comprised of gas, mostly hydrogen and helium. Some of this gas eventually turns into stars during structure formation. Astrophysical gases in cosmological simulations are typically described as inviscid ideal gases following the Euler equations, which can be expressed in different forms leading to different numerical discretization schemes.

$$\frac{\partial \rho}{\partial t} + \nabla \cdot (\rho \mathrm{v}) = 0, \tag{1.4}$$

$$\frac{\partial \rho \mathrm{v}}{\partial t} + \nabla \cdot (\rho \mathrm{v} \otimes \mathrm{v} + p) = 0, \tag{1.5}$$

$$\frac{\partial \rho E}{\partial t} + \nabla \cdot (\rho E + p)\mathrm{v} = 0, \tag{1.6}$$

where $E = e + \mathrm{v}^2/2$ is the total energy per unit mass, e is the internal energy, ρ is the matter density, $\mathbf{v}$ is the velocity vector, and $p = (\gamma - 1)\rho e$ with $\gamma = 5/3$ is the pressure.

Hydrodynamics in cosmological simulations is numerically demanding due to the large dynamic range, highly supersonic flows, and large Reynolds numbers. The hydrodynamical equations can be discretized in different ways employing methods that roughly fall into three classes: Lagrangian, Eulerian or arbitrary Lagrange-Eulerian techniques. The Lagrangian specification of the field assumes an observer that follows an individual fluid parcel, with its own properties like density, as it moves through space and time. The Eulerian specification, on the other hand, focuses on specific locations in space through which the fluid flows as time passes. In addition, numerical approaches can also be distinguished between mesh-free and

mesh-based algorithms. Mesh-free methods do not require connections between nodes, but are rather based on interactions of each node with its neighbors.

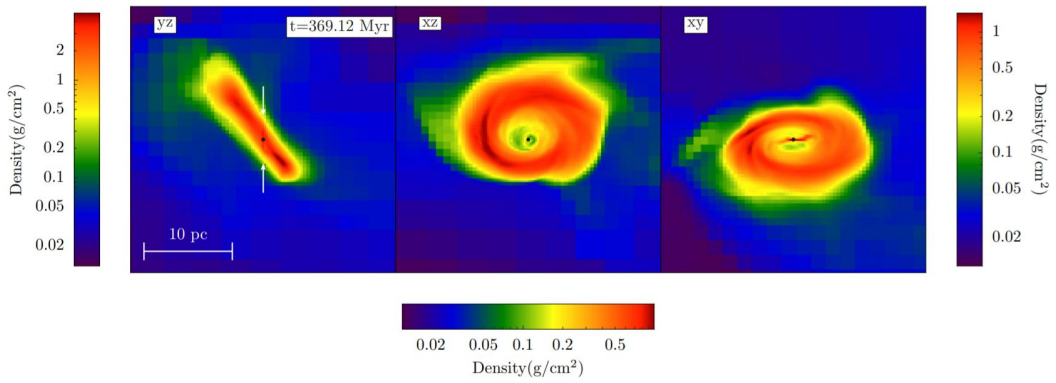

FIGURE 1.5: Gas column density normal to main planes at the end of the simulation. The left frame shows the inner edge-on disk (position delineated by the white arrows) embedded in the outer disk. The middle frame shows the same figure with the inner disk being face-on. The right frame shows another projection of the inner edge-on disk and the inclined (toward the observer) outer disk (Shlosman et al. 2016).

Cosmological simulations include models for supermassive black holes, and numerically seed them typically in dark matter haloes with masses $\gtrsim 10^{10} - 10^{11} M_{\odot}$ since the true seeds cannot be resolved, and their origin is not yet fully understood. They then accrete mass often based on an Eddington-rate-capped Bondi-Hoyle-like accretion rate: $\dot{M}_{\rm BH} = (4\pi G^2 M_{\rm BH}^2 \rho)/(c_s^2 + v_{\rm rel}^2)^{3/2}$, where ρ and c_s are the gas density and gas sound speed, respectively, and $v_{\rm rel}$ denotes the relative velocity between the gas and the black hole. Depending on the numerical resolution this accretion rate is sometimes artificially increased, possibly in a density-dependent fashion, to compensate for the inability of simulations to resolve the multi-phase structure of gas (Booth and Schaye 2009). The problem with these simulations is that due to their large scale, the resolution power of the central object is limited. We can see that a galaxy-size simulation (shown in Figure 1.5) can only trace the gas to $r \sim 0.1$pc. Continuing to trace the gas further would result in a simulation to taxing to compute. The method these simulations use then, is to place a "sink" particle of size equal to the minimum resolution where all matter that passes that threshold is considered accreted.

This presents a few challenges, the first being that an assumption of a 100% accretion rate efficiency, will lead to an overestimation of the growth rate of the central particle. Not only that, but we also have the fact that assuming no outflow, implies no AGN feedback. From observations (see last section), we have discussed how SMBHs at the center of galaxies present some of the most bright MeV quasars. Thus the assumption of not outflow, no feedback, from the central particle is not very realistic.

This is further supported by other cosmological studies like Debuhr, Quataert, and Ma (2012), where they assume a simplified model of the wind produced by the AGN and compare the changes to the simulation. We can see from Figure 1.6, that in a sub-Eddington accretion flow model, the outflow produced is enough to clear the gas out of the orbital plane. He have already mentioned that in high-z scenarios the

super-Eddington flow is more likely, thus this simplified flow will not be adequate in this study.

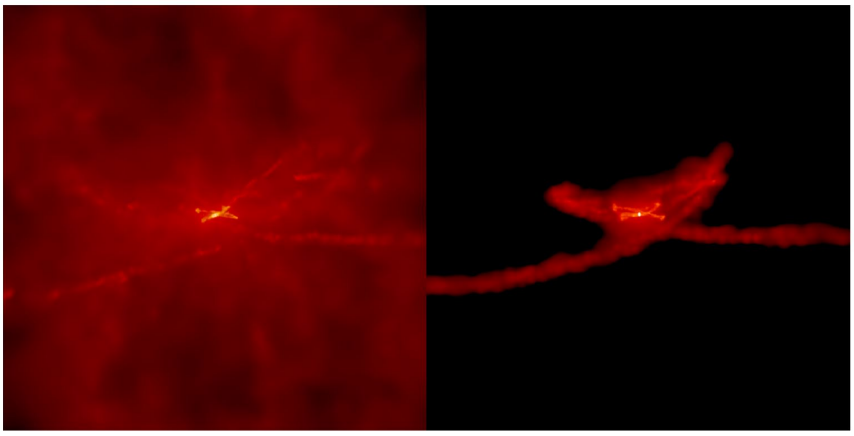

FIGURE 1.6: The projected gas density for the fiducial simulation (left) and the run without AGN wind feedback (right) at a time just after the final merger (t = 1.71 Gyr). Brighter color corresponds to higher density. (Debuhr, Quataert, and Ma 2012).

The problem that cosmological simulations have, is their limitation in resolution close the the central BH. And due to that these studies need to resort to approximations and assumptions for and around the AGN. This can work for certain studies, but to shed a light on the processes behind SMBH formation and evolution, they are not sufficient.

1.4 Studying SMBHs through astrophysical simulations

The other tool, to analyze the evolution of SMBHs, that we need to introduce are astrophysical simulations. These simulations are focused on the study of accretion gas dynamics around the AGNs (e.g. Eggum, Coroniti, and Katz 1987, Matsumoto 1999, Hawley and Choptuik 2000, Machida and Matsumoto 2000, Dubois et al. 2015). These ones provide information of the infall and outflow structure though radiation hydrodynamic (RHD), magnetohydrodynamic (MHD) or general relativistic magnetohydrodynamic (GRMHD) physics. Starting with the MHD simulations, due to their capacity to offer an approach based on unified view of various common active phenomena, such as jets, outflows, flares, bursts, they are crucial tools in astrophysics (see Figure 1.7).

Like any model there are some approximations that need to be taken for MHD simulations to work. First is the so-called hydrodynamic approximation, where the characteristic length (L) needs to be much larger than the mean free path (λ), or ion Larmor radius. By requiring this they can speed the process by disregarding kinetic treatment of local perturbations of the medium. The second requirement that must be met is a slow timescale, where the displacement current is neglected (i.e. non-relativistic approximation). In this approximation the characteristic timescale (t) must be much larger than the collision time (t_{coll}). Lastly, they must satisfy the Quasi-Neutrality condition, where the particle number density $\gg$ Goldreich-Julian density $\gg n_0$ ($n = \nabla \cdot (v \times B)/e$). With these approximations taken one can then solve the set of MHD equations:
The mass equation

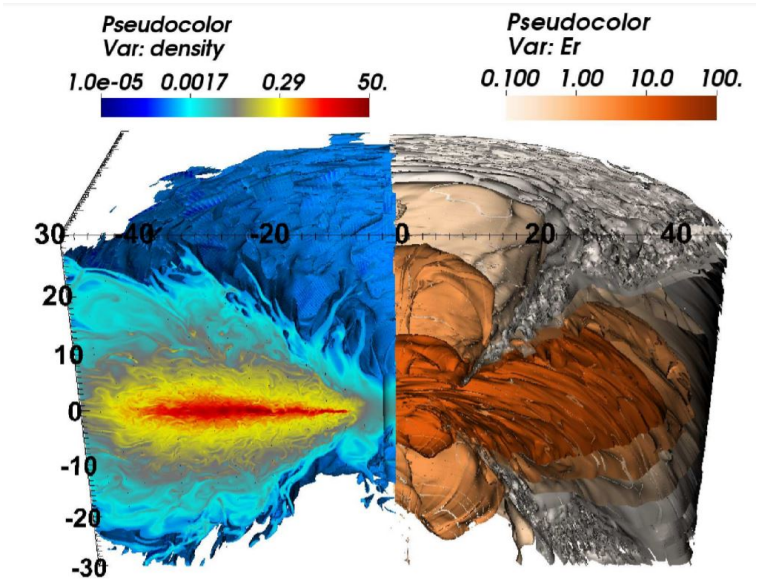

FIGURE 1.7: Snapshot of disk structures for density (left) and radiation energy density (right) of black hole accretion disk based on first principle 3D radiation MHD simulations (Jiang, Stone, and Davis 2014).

$$\frac{\partial \rho}{\partial t} + \nabla \cdot (\rho v) = 0, \tag{1.7}$$

the momentum equation

$$\rho \frac{dv}{dt} + \nabla p = \frac{1}{c} J \times B, \tag{1.8}$$

the energy equation

$$\rho \frac{d}{dt}\left(\frac{p}{(\gamma - 1)p}\right) + p \nabla \cdot v = \frac{1}{\sigma} J^2, \tag{1.9}$$

and lastly the induction equation

$$\frac{\partial B}{\partial t} = \nabla \times \left(v \times B - \frac{c}{\sigma} J\right). \tag{1.10}$$

here B is the magnetic field and J is the current density defined as $J \propto \nabla \times B$.

However, for the purpose of the study of BH accretion physics and AGN feedback MHD simulations are not enough. There are several reasons for why the ideal MHD equations do not suffice:

- Light speed does not appear explicitly, thus we can not know if the jet near the black hole (BH) is relativistic or not.
- No energy and mass equivalency.
- No Lorentz contraction and momentum of energy and fields.
- No of general relativistic effects, e.g. extremely strong gravity, frame-dragging effect, and gravitational red-shift.

Thus a modification to introduce the relativistic effects near these objects must also be considered. By introducing some changes to the ideal MHD equations (e.g., gravitational red-shift, solution of Einstein equation through Schwarzschild or Kerr's metric, ...) one can obtain a new set of equations that include the relativistic behaviour. This allows for much closer simulations of gas accretion in to the central particle (see Figure 1.8) .

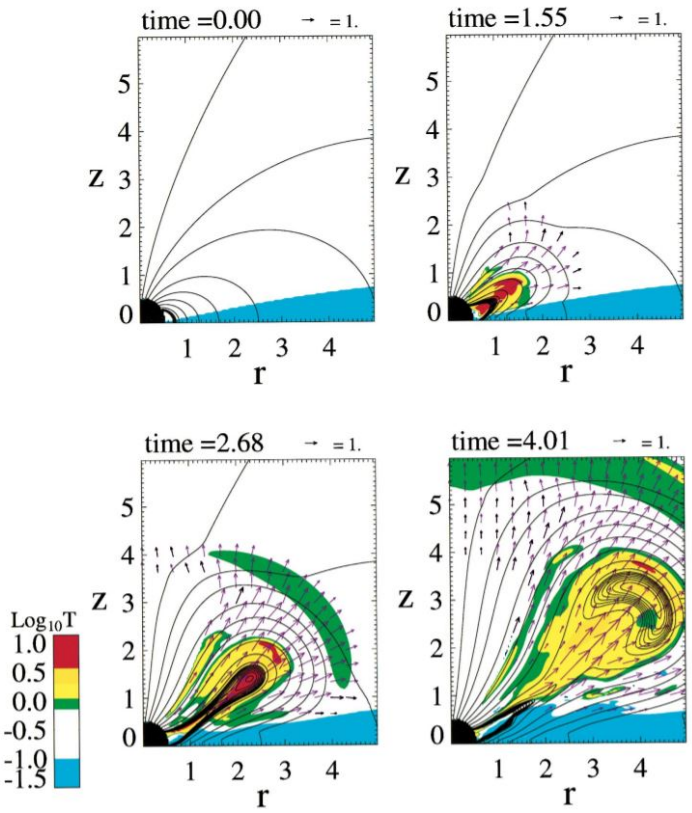

FIGURE 1.8: Result of the numerical simulation for a model of the mass outflow driven by magnetic interaction between a protostar and its surrounding disk. Solid curves denote magnetic field lines. (Hayashi, Shibata, and Matsumoto 1996).

The problem with MHD and GRMHD simulations, when used for the study of AGN accretion and outflow impact, is that they do not include the gas/radiation interaction. To estimate the importance of radiation in fixing the local properties of a radiating fluid, we can use the ratio R of the material internal energy density $\hat{e}$ to the radiation energy density E; for a perfect gas-radiation equilibrium:

$$R \equiv \hat{e}/E = (3k_{\rm B}/2a_r)(N/T^3). \tag{1.11}$$

We should note that R also gives a measure of the relative importance of gas and radiation pressure because $p = \frac{2}{3}\hat{e}$ for a perfect gas, and $P = \frac{1}{3}E$ for radiation. Clearly radiation is most important at high temperatures and/or low densities. In the particular case of accretion disks and AGN jets, due to the small density ($\rho < 10^{-10}$g cm^{-3}) and high temperatures ($T \gg 10^4 K$) radiation is overwhelmingly important. Even more, gas-radiation interaction should be critical in the particular case of super-Eddington accretion, that inevitably appears when the mass of BH seeds are small, and as we have already discussed should be even more prevalent in a high-z scenario.

This leads us to the last of the astrophysical simulations to appear and the ones this project will center around are the radiation hydrodynamic simulations (RHD). A fluid interacting with electromagnetic radiation gains or loses energy and momentum through the emission, absorption and scattering of photons (see Figure 1.9). Radiation hydrodynamics is a set of techniques used to model the resulting flows. The intensity of the radiation field and the optical depth of the fluid determine many basic properties of the composite system, and are key factors to consider in choosing a modeling approach.

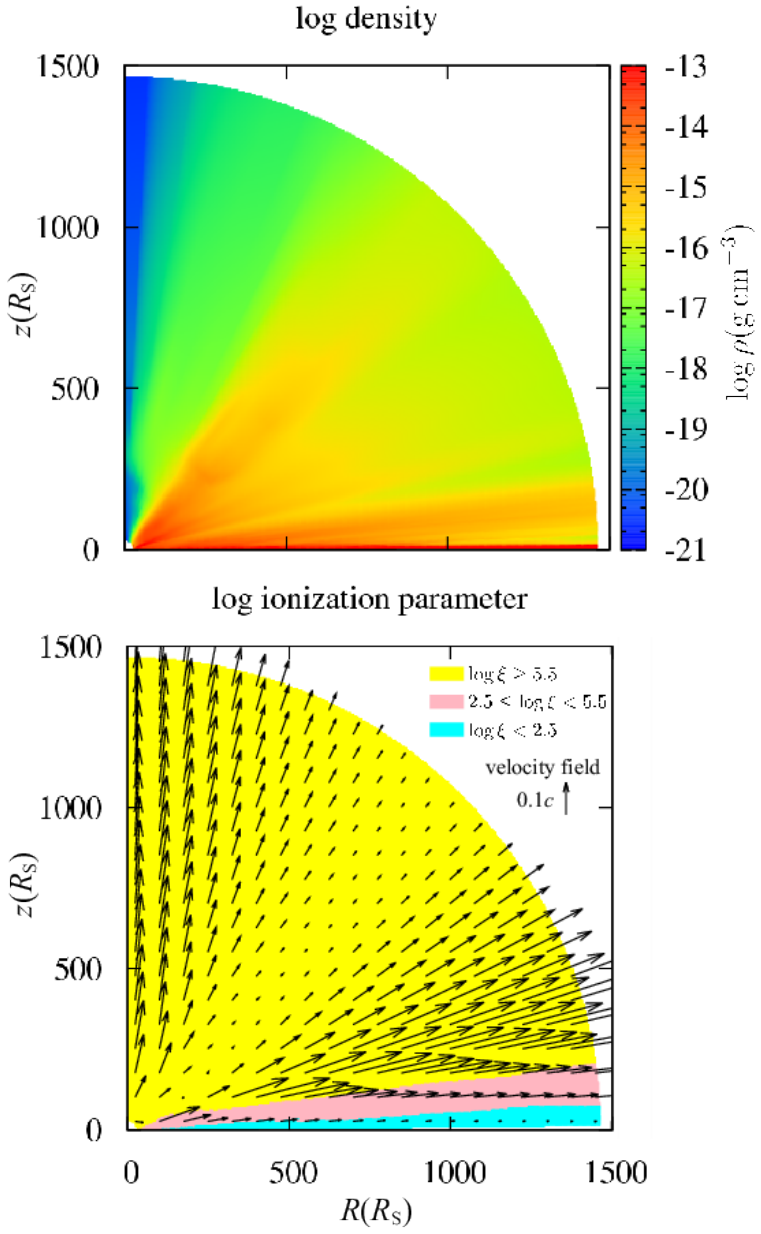

FIGURE 1.9: Result of an RHD numerical simulation of gas being accreted into a BH of mass $M_{BH} = 10^8 M_\odot$. Time averaged density map (top panel) and the ionization parameter map (bottom panel) (Nomura et al. 2016).

In these simulations the interaction between the gas and the radiation field drives

the evolution of the study in addition to the magnetic fields like in the aforementioned studies. Because we will be using an RHD code for our project, these simulations will be explained in more detail in Chapter 2. Through RHD simulations we create highly precise images of the gas interaction with the central object (e.g. Eggum, Coroniti, and Katz 1987, Eggum, Coroniti, and Katz 1988, Kley 1989, Okuda, Fujita, and Sakashita 1997, Fujita and Okuda 1998, Kley and Lin 1999, and Okuda and Fujita 2000). Through them we can calculate the more precise rates of mass growth for the AGN as well as the strength of the outflow. RHD simulations were done first in Newtonian dynamics (e.g. Ohsuga et al. 2009, Ohsuga and Mineshige 2011; Kawashima et al. 2009; Jiang, Stone, and Davis 2014, Jiang, Stone, and Davis 2019) and later general relativistic treatment was introduced (e.g. McKinney et al. 2014; Sądowski et al. 2015, Sądowski and Narayan 2016; Takahashi et al. 2016). These simulations due to not including the magneto-hydrodynamic interaction need to rely on the phenomenological α-viscosity model.

But similarly to the other types of simulations, these also suffer from resource limitations. Due to resolution limitations, we cannot solve the small-scale and large-scale structure simultaneously with good accuracy. This is due to the need to resolve the RHD equations (see Chapter 2) numerically. The larger the simulation box size is, and/or the smaller the resolution, the longer the simulation time becomes. In addition, to study the gas dynamics far enough from the central AGN, one needs to consider the change in the chemistry of the gas (e.g. Takeo et al. 2019; Takeo, Inayoshi, and Mineshige 2020), which adds extra complexity to the equations.

Lastly, we have the more complete BH simulations which are the RMHD and even GR-RMHD simulations. These studies as the name indicates combine the magneto(or general relativistic magneto)hydrodynamics with the radiation feedback. This method was previously used in some works (e.g.,Turner et al. 2003, Hirose, Krolik, and Stone 2006) with some limitations. Later this method was expanded in Ohsuga et al. (2009) and Ohsuga and Mineshige (2011) to make multi dimensional RMHD simulations around the BH. These studies offer an indepth view on the accretion and outflow structure and evolution near the BH. However, if the RHD were limited on the size of the box, these more complete RMHD simulations are even more costly. Beyond that, since we are interested, not in the physics near the AGN but its impact in the cosmological scale the magnetic(or general relativistic magnetic) part becomes irrelevant.

Due to all these factors mentioned above, BH simulations, as their cosmological counterpart, are also rendered inadequate for tackling the SMBH growth question.

1.5 Super-Eddington flow

We have mentioned how in the early universe we have the ideal conditions for super-Eddington flow to occur. This is crucial since, if we want to study SMBH growth and the wind they generate, we need to study these AGN under the conditions we would find them at. Thus we need to understand better the implications of the Super-Eddington flow.

The Eddington luminosity, also referred to as the Eddington limit, defined as the value the force of the outward acting radiation must have to balance the inward acting gravitational pull. This is hydrostatic equilibrium gives us an pseudo-upper limit for the intensity of the accretion rate into a BH. This limit however can be overcome through relativistic effects when the conditions are met. In the scenarios when this limit is breached we have what is know as Super-Eddington flow.

The concept behind this higher accretion flow, is that due to a very strong accretion process, the optical depth of the disk becomes larger. This means that photons diffusion will take longer and at a certain limit these photons can be trapped within gas flow and swallowed by a central black hole together with gas. This is what we call the photon-trapping effect, and it is one way to enhance accretion past the Eddington limit.

To implement this concept in the RHD simulations we will use what is known as the slim disk model. The slim disk model is a numerical model, obtained by Watarai, Mizuno, and Mineshige (2001), in which the photon-trapping effect is included as the advection of the photon entropy in the energy equation.

Super-Eddington accretion flow also has an impact on the outflow produced by the central object. Having a super-Eddington luminosity means, that the radiation force is greater than the gravitational force, which, as mentioned before, leads to radiation-pressure driven outflow (Shakura and Sunyaev 1973). This is a very important effect since such an outflow will have an inevitable impact on the environments far from the central black hole.

The last important effect of a BH under super-Eddington flow that we will talk about here is the Compton scattering. We can see in Kawashima et al. (2009) that when including Compton scattering in the RHD simulations, the outflow, but not the inflow, is modified. In particularly they found, that due to the presence of the scattering temperatures of the outflow dropped, together with the density. This in turn created a weaker outflow rate with a slightly increase in the accretion rate.

These are not the only effects super-Eddington accretion flows introduce but are some of the more relevant to the discussion. And we can see why is it so important for the discussion of growth and outflow structure around SMBH at high-z. And introducing this effect to the study adds complex radiation-matter interactions which can only be solved numerically.

1.6 Objectives and structure of our work

The main objectives of this project are two-fold: the first one is to study the growth of SMBH at high-z under different conditions to better understand the mechanisms involved, and the second one is to obtain a complete model of the escaping outflow from these AGN and study the impact they will make on the surrounding medium.

The motivation behind this project is to be able to bridge the gap between cosmological and astrophysical simulations. As we have discussed the former ones are capable of a very large simulation boxes covering entire sections of the universe. They fail, however, since they cannot resolve the flow structure in the BH vicinity. Their inability of following the gas down to a certain distance from the central object leads them to take assumptions. The latter ones (astrophysical simulations), on the other hand, can obtain very precise and reliable models of the gas behaviour near the BH. But extending such precise simulations, to the cosmological scale, concurs a tremendous computational cost. Thus there is no clear way (beyond approximations and rough extrapolations) of combining both results. In this project we wish to cover this information void and obtain a more realistic accretion rate and outflow impact by AGN at high-z.

In order to perform such a study, we need to perform a simulation capable of tracing the gas between the BH boundary (i.e. $\sim r_{\rm Sch}$) and the inner cosmological boundary (i.e. $\sim 10^{9-10}\ r_{\rm Sch}$, for PopIII star seeds). Covering $\sim 9-10$ orders of magnitude in radius in a single simulation box, while having enough resolution, is

impossible. Through non of the aforementioned simulation methods (cosmological, GRMHD or RHD) can one created such an intricate scenario.

Previous work trying to bridge the gap between BH accretion and galactic simulations has been attempted before but with limitations. The simulations performed in Yuan, Wu, and Bu (2012) obtained a 2D mapping of hydrodynamics and MHD evolution of the gas. These simulations covered around 4 orders of magnitude in length scale by iterating the results between different-size simulation boxes. Ressler, Quataert, and Stone (2020) performed the 3D-GRMHD simulations of Sgr A* by solving simulation from larger scale to smaller scale covering over 3 orders of magnitude, but they did not include the radiation impact.

Since the purpose remains to have a simulation capable of covering gas dynamics until the BH boundary RHD codes offer us the best tools. With that in mind we will need to develop a new method to use the RHD code in a manner to both simulate such a large box (we will see in Chapter 3 that we can, in fact, use a smaller simulation box), and maintain the simulation cost at a reasonable range.

We will explain how the RHD code works in more detail in Chapter 2, where we will also show and explain the modifications needed to adapt the original code to this problem. In Chapter 3 we will showcase this new tool by applying it to our fiducial model. In Chapter 4 we will present how the results are affected when the injection rate is modified. And lastly in Chapter 5 we will present the conclusions that we can draw from this project.

Chapter 2

Models and Numerical Methods

For this study we will use the simulation code developed by (Kawashima et al. 2009, Ohsuga et al. 2005 (Oshg+05)) as a basis to build our tool. In this code a full set of axisymmetric two-dimensional RHD equations including the viscosity term are solved. The flux-limited diffusion (FLD) approximation is adopted (Levermore and Pomraning 1981; Turner and Stone 2001). We also adopt the α-viscosity prescription (Shakura and Sunyaev 1973). General relativistic effects are incorporated by adopting the pseudo-Newtonian potential $\Psi(r) = -GM/(r - r_{\rm Sch})$ (Paczyński and Wiita 1980). Here, we assume that intermediate mass black holes are appropriate seeds of SMBHs, so that the mass of the central black hole is set to be $10^3 M_\odot$.

In this chapter we will explain in detail the basic equations to solve the gas-radiation interaction and evolution through Oshg+05 RHD code. We will also explain what our new method entails and how we modified the boundary conditions according to the nested-simulation box method.

2.1 RHD equations

This 2D-RHD code solves the axisymmetric two-dimensional radiation hydrodynamic equations in the spherical coordinates $(x, y, z) = (r\sin\theta\cos\varphi, r\sin\theta\sin\varphi, r\cos\theta)$, where the azimuthal angle φ is set to be constant. We put a black hole with mass of BH at the origin. This coupled with other assumptions, non self-gravitating flow, reflection symmetric relative to the equatorial plane (with $\theta = \pi/2$), and axisymmetry with respect to the rotation axis (i.e., $\partial/\partial\varphi = 0$) creates a complete simplified set of the basic equations.

The continuity equation is:

$$\frac{\partial\rho}{\partial t} + \nabla\cdot(\rho\boldsymbol{v}) = 0. \tag{2.1}$$

Here, ρ is the gas mass density and $\boldsymbol{v} = (v_r, v_\theta, v_\varphi)$ is the velocity of gas.

The equations of motion are:

$$\frac{\partial(\rho v_r)}{\partial t} + \nabla\cdot(\rho v_r\boldsymbol{v}) = -\frac{\partial p}{\partial r} + \rho\left(\frac{v_\theta^2}{r} + \frac{v_\varphi^2}{r} - \frac{GM_{\rm BH}}{(r - r_{\rm Sch})^2}\right) + \frac{\chi}{c}F_{0,r}, \tag{2.2}$$

$$\frac{\partial(\rho r v_\theta)}{\partial t} + \nabla\cdot(\rho r v_\theta\boldsymbol{v}) = -\frac{\partial p}{\partial\theta} + \rho v_\varphi^2\cot\theta + r\frac{\chi}{c}F_{0,\theta}, \tag{2.3}$$

$$\frac{\partial(\rho r\sin\theta v_\varphi)}{\partial t} + \nabla\cdot(\rho r\sin\theta v_\varphi\boldsymbol{v}) = \frac{1}{r^2}\frac{\partial}{\partial r}\left(r^3\sin\theta t_{r\varphi}\right). \tag{2.4}$$

Here p is the gas pressure, $\chi = \kappa + \rho\sigma_{\rm T}/m_{\rm p}$ is the total opacity, κ is the free-free and bound-free absorption opacity (Rybicki and Lightman 1986), $\sigma_{\rm T}$ is the cross-section of Thomson scattering, $m_{\rm p}$ is the proton mass, and $F_0 = (F_{0,r}, F_{0,\theta}, F_{0,\phi})$ is the radiative flux in the comoving frame, where the suffix 0 represents quantities in the comoving frame. We set $F_{0,\phi} = 0$ because of the axisymmetry.

The radiative flux, F_0, is connected to the radiation energy density in the comoving frame, E_0, by the flux-limited diffusion approximation (Levermore and Pomraning 1981; Turner and Stone 2001), defined as:

$$F_0 = -\frac{c\lambda}{\chi}\nabla E_0, \tag{2.5}$$

with the flux limiter, λ as:

$$\lambda = \frac{2 + R_{\rm FLD}}{6 + 3R_{\rm FLD} + R_{\rm FLD}^2}, \tag{2.6}$$

$$R_{\rm FLD} \equiv \frac{|\nabla E_0|}{\chi E_0} \tag{2.7}$$

We assume that only the r-ϕ component of the viscous-shear tensor is nonzero, and it is prescribed as

$$t_{r,\phi} = \eta_r \frac{\partial}{\partial r}\left(\frac{v_\phi}{r}\right), \tag{2.8}$$

with the dynamical viscous coefficient being:

$$\eta_r = \rho\nu = \alpha\frac{p + \lambda E_0}{\Omega_{\rm K}}. \tag{2.9}$$

Here, $\alpha = 0.1$ is the α parameter (Shakura and Sunyaev 1973), Ω_K is the Keplerian angular speed.

The energy equation of the gas is:

$$\frac{\partial e}{\partial t} + \nabla\cdot(e\boldsymbol{v}) = -p\nabla\cdot\boldsymbol{v} - 4\pi\kappa B + c\kappa E_0 + \Phi_{\rm vis} - \Gamma_{\rm Comp}, \tag{2.10}$$

and the energy equation of the radiation is:

$$\frac{\partial E_0}{\partial t} + \nabla\cdot(E_0\boldsymbol{v}) = -\nabla\cdot\mathbf{F}_0 - \nabla\boldsymbol{v} : \mathbf{P}_0 + 4\pi\kappa B - c\kappa E_0 + \Gamma_{\rm Comp}. \tag{2.11}$$

Here, e is the internal energy density which is linked to the thermal pressure by the ideal gas equation of state, $p = (\gamma - 1)e = \rho k_{\rm B} T_{\rm gas}/(\mu m_{\rm p})$ with $\gamma = 5/3$ being the specific heat ratio, $k_{\rm B}$ the Boltzmann constant, $\mu = 0.5$ is the mean molecular weight (we assume pure hydrogen plasma), and $T_{\rm gas}$ is the gas temperature. $B = \sigma_{\rm SB} T_{\rm gas}^4/\pi$ is the blackbody intensity where $\sigma_{\rm SB}$ is the Stefan–Boltzmann constant, P_0 is the radiation pressure tensor, $\Phi_{\rm vis}$ is the viscous dissipative function written as:

$$\Phi_{\rm vis} = \eta_r\left[r\frac{\partial}{\partial r}\left(\frac{v_\phi}{r}\right)\right]^2. \tag{2.12}$$

The Compton cooling/heating rate $\Gamma_{\rm Comp}$ is described as

$$\Gamma_{\rm Comp} = 4\sigma_T c\frac{k_{\rm B}(T_{\rm gas} - T_{\rm rad})}{m_{\rm e}c^2}\left(\frac{\rho}{m_{\rm p}}\right)E_0. \tag{2.13}$$

For these equations, m_e is the electron mass and $T_{rad} \equiv (E_0/a_r)^{1/4}$ is the radiation temperature with the radiation constant $a_r = 4\sigma_{SB}/c$.

The radiation pressure tensor, $\boldsymbol{P}_0$, in the flux-limited diffusion approximation is represented by:

$$\boldsymbol{P}_0 = \boldsymbol{f} E_0 \tag{2.14}$$

$$\boldsymbol{f} = \frac{1-f}{2}\boldsymbol{I} + \frac{3f-1}{2}\boldsymbol{nn}, \tag{2.15}$$

$$n \equiv \frac{\nabla E_0}{|\nabla E_0|}, \tag{2.16}$$

$$f = \lambda + \lambda^2 R_{FLD}^2 \tag{2.17}$$

2.2 Nested simulation-box method

Now that we have a better understanding of the physics involved in the 2D RHD simulation code, we can introduce the method developed in this project named: **Nested Simulation-Box** method.

As we have mentioned the objective for the development of this method is to study the gas and radiation produced by an AGN onto the galactic medium. In order to quantitatively address the effects of the mechanical and radiative feedback the cosmological scale fluid, the outer boundary should be placed at $r \sim 0.1\text{pc} \sim 10^9\, r_{Sch}(M_{BH}/10^3 M_\odot)^{-1}$. This is obtained by the innermost limit on galactic simulations (e.g., Shlosman et al. 2016), where the studies can no longer follow the gas evolution (see Chapter 1). We will, however, set the outer boundary at $r = 10^6 r_{Sch}$. This is because we found that this value for the radius is far enough from the black hole to evaluate the feedback effects (see Chapter 3 for the extended explanation).

Since the simulation box still covers an enormous length scale, a single simulation box is incapable of computing the gas dynamics in a reasonable time. Thus, we need to implement a suitable method by extending our RHD code, i.e. the Nested Simulation-Box method. Our method consists of a series of simulation boxes tied together to give a sense of zoom-out/zoom-in. How this zooming effect works is that the information is passed from one simulation box to the next one through boundary conditions. This allows us to trace the evolution of the inflow and outflow at different scales with maximum resolution and minimum computational cost.

For the cases discussed in our work we prepared two zones: inner and outer zones (Table 2.1 and Figure 2.1), and perform simulations in these two stages.

Stage	Zone	r_{in} [r_{Sch}]	r_{out} [r_{Sch}]	Simulated flow
1^{st}	Inner	2	3×10^3	inflow & outflow
2^{nd}	Outer	2×10^3	3×10^6	outflow

TABLE 2.1: Naming convention for the stages in the nested box method for the simulation discussed in this paper.

The boundary conditions of these 2 simulation boxes are as follows:

- 1^{st} stage inner boundary: Absorbing inner boundary (see Ohsg+05).

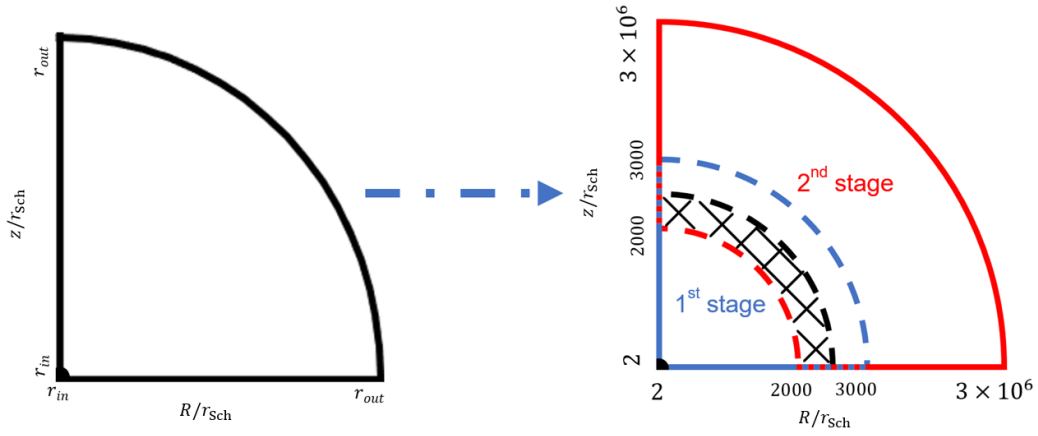

FIGURE 2.1: Schematic example of the nested simulation box method. The initial box (left) is separated into 2 smaller boxes (right), i.e., 1^{st} stage (blue delimited area) ($2 < R/r_{Sch} < 3000$) and 2^{nd} stage (red delimited area) ($2000 < R/r_{Sch} < 3 \times 10^6$). The black marked area represents the connection zone shared between 1^{st} to 2^{nd} stage as boundary condition ($2000 < R/r_{Sch} < 2500$). The remainder of the shared space will be used to determine the consistency between stages.

- 1^{st} stage outer boundary: Free boundary (i.e., gas can escape the box), with inflow input through the equatorial plane as explained in the previous section (see also Ohsg+05).
- 2^{nd} stage inner boundary: Connection zone to incorporate the results of 1^{st} simulation (will be discussed next)
- 2^{nd} stage outer boundary: Free boundary (i.e., gas can escape the box).

The Nested Simulation-Box method however is not limited to 2 boxes, we can technically keep placing simulation boxes to extend the total computational box. However, for the cases studied here this is not needed. It is also important to notice that the sizes of each simulation are not chosen at random, we will see in Chapter 3 how for some scenarios smaller/bigger boxes would affect the results.

So, how do we create a smooth connection between the two stages? The first step in this connection process is to take a set of time dependent variables of the gas and radiation (i.e., density, velocity vector, gas and radiation energy) at the moment when the 1^{st} stage simulation has achieved quasi-steady state (t_{qs}). We then time-average the physical variables (ρ, v, E_{gas}, E_0) for $2000r_{Sch} \leq r \leq 2500r_{Sch}$ for $0 \leq \theta < \pi/2$. This is to ensure a smooth connection between stages.

Because of how the simulation boxes are chosen, and the fact that we are only concerned with outflow properties to study AGN feedback, we do not consider inflow gas in the 2^{nd} simulation. This can be done without a problem due to 2 reasons:

- By choosing $r_{out}^{1st} \gg r_{Kep}$ the gas falling from the outermost boundary will pass in a free-fall like scenario through the 2^{nd} stage. (Here, r_{Kep} is the Keplerian radius, at which the centrifugal force, with a given specific angular momentum, is balanced with the central gravity) Thus making this stage irrelevant.

- Due to the very large density gap between the inflow disk and outflow gas ($\sim$ 4 orders of magnitude), outflow does not alter the inflow process in the 2^{nd} stage.

By eliminating the inflow region from the 2^{nd} stage we also can save on the computational cost. But how do we eliminate the inflow region, in a natural way, if the inflow region is present on the connection region?

The technique we used to eliminate the inflow section in the 2^{nd} stage was a re-scale of the physical values in the connection zone (i.e., the black marked area in Figure 2.1 covering $2000r_{\rm Sch} < r < 2500r_{\rm Sch}$). What we do is re-define the azimuthal angle (θ) for $\theta > \theta_{\rm ah}$, with $\theta_{\rm ah}$ defined as the angular height of the inflow-outflow interface in the connection zone defined by $\theta | v_r(\theta) = 0$. We set a gradual remapping of the values in the connection zone such that at the inner boundary of the 2^{nd} stage (at $r = r_1 = 2000r_{\rm Sch}$):

$$x^{\rm 2nd}(r_1, \theta) = x^{\rm 1st}(r_1, \theta) \text{ for } 0 < \theta < \pi/2, \tag{2.18}$$

but at the outer boundary of the connection zone (at $r = r_n = 2500r_{\rm Sch}$):

$$x^{\rm 2nd}(r_n, \theta*) = x^{\rm 1st}(r_n, \theta) \text{ for } 0 < \theta < \pi/2 \tag{2.19}$$

Here $\theta* = \pi/2\,(\theta/\theta_{\rm ah})$, x represents the time-averaged hydrodynamic variables ($\rho, v, E_{\rm gas}$) and the super-index indicates the stage. This eliminates the inflow area by "stretching" the surrounding outflow values thus effectively remapping the inflow to grid points outside the simulation box.

The same method is employed for the radiation energy. The inner boundary condition in the 2^{nd} simulation is set so as to also recreate the radiation profile seen in the previous stage (i.e., we no longer adopt the absorbing boundary used in the 1st simulation). The radiation flux is then solved from radiation energy through the FLD method.

Outside the connection zone of the 2 simulation boxes, we also need to implement other changes to the core program to better adapt it to this 2^{nd} stage.

One of the things we also need to consider is that, the farther away from the black hole one places the gas, the colder it will be. This basic radiation trend means the gas may cool down bellow the $T = 10^4$K. This means that the approximation taken previously of the gas being fully ionized no longer stands true. This introduces new dispersion factors with the introduction of b-f interactions. In order to introduce this new factor to the code we added a modifier to the opacity factor:

$$\kappa' = \kappa \times \left(\frac{\tanh\left(\frac{T_{\rm gas} - T_{\rm ion}}{\tau}\right) + 1}{2} \right), \tag{2.20}$$

where $T_{\rm ion} = 10^4$K, and $\tau = 2 \times 10^3$K is a transition factor between the f-f and the b-f phase. This is necessary since when $T < 10^4$K the hydrogen is not-ionized. Therefore, the amount of the free electrons is smaller in this scenario, and the effective scattering opacity should become small.

2.3 Initial set-up

We assume an atmosphere that is hot, optically thin, isothermal and in hydrostatic equilibrium in the radial direction, with negligible mass around the black hole, in

a similar fashion to the results presented in Ohsg+2005. The coronal gas is set in such a way that its atmospheric pressure does not impede gas flow, thus we start the simulation with $T_{\rm gas} = 10^{11}$ K and $\rho = 10^{-17}$g cm^{-3}.

In the 1st stage simulation, the matter is injected from the outer boundary near the equatorial plane with $1.5 < \theta \leq \pi/2$. The cases presented here are characterized by different initial conditions (see Table 2.2).

Model	**Angular Momentum**	**Mass Accretion Rate**	**Chapter**
Low-Angular Momentum	100 $[r_{\rm Sch}]$	1000 $[L_{\rm Edd}/c^2]$	3
Reduced Injection	100 $[r_{\rm Sch}]$	500 $[L_{\rm Edd}/c^2]$	4

TABLE 2.2: Initial condition set-up for the different models presented in this project.

In the 2^{nd} stage simulation, the initial conditions of the coronal gas are taken as a thinner and much colder gas ($\rho = 10^{-21}$g cm^{-3} and $T_{\rm gas} = 10^4$ K). The mass and radiation are injected from the connection zone near the inner boundary as is described in the section 2.2.

Before moving onto the results section it is worth explaining why we only use 2 stages with the outermost boundary placed at $r = 3 \times 10^6 r_{\rm Sch}$. We found that for the particular cases discussed here, any outflow wind that reaches this distance will be from the influence of the BH. Once this happens we can confidently extrapolate that the structure will follow the same radial trends from that point on. This makes subsequent further simulation boxes redundant and unnecessary (as will be discussed in Chapter 3).

Chapter 3

Fiducial model

In this section we will present the results from the simulations performed with the nested simulation-box method for the first model in Table 2.2. This is the first model we tested out method with. The low angular momentum provides a very fast evolving framework that accelerates simulation time. One important thing to understand through this first set of results is that, while it may be a more idealistic model it still provides a strong setting to test our method.

The results will be presented starting with the inflow part and then the outflow part. For the following results we will use the naming convention established in Table 2.1. To save computation time, we assume symmetry of the flow structure with respect to the equatorial plane; namely, we have chosen $\theta \in \{0 - \pi/2\}$, in which $\theta = 0$ (or $\pi/2$) corresponds to the rotation axis (the equatorial plane).

3.1 Inflow

In the first stage, the injected gas from the outer boundary rapidly falls unimpeded in a free-fall. This will continue all the way down to the region around the Keplerian radius, $r_{\rm Kep} = 100 r_{\rm Sch}$). Then, viscous (slow) accretion process starts. Because of this free-fall nature down to the Keplarian radius, the gas can be initiated at the 1^{st} stage without altering the results.

From Figure 3.1 (which shows time variations of the mass accretion rate onto the BH) we can see how the BH mass grows over time. While the mass flux shows fluctuations over time, we see that its time average settles down in a constant value at later times, indicating that a quasi-steady state is achieved. Since the flow must be in the quasi-steady state before proceeding to the next stage simulation, we need to confirm if it is indeed the case. This can be done by looking at the mass flux profiles calculated as follows:

$$\dot{M}_{\rm in}(r) \equiv 4\pi \int_0^{\pi/2} \sin\theta \times r^2 \rho(r,\theta) \min\{v_r(r,\theta), 0\} d\theta, \tag{3.1}$$

$$\dot{M}_{\rm out}(r) \equiv 4\pi \int_0^{\pi/2} \sin\theta \times r^2 \rho(r,\theta) \max\{v_r(r,\theta), 0\} d\theta, \tag{3.2}$$

$$\dot{M}_{\rm esc}(r) \equiv 4\pi \int_0^{\pi/2} \sin\theta \times r^2 \rho(r,\theta) v_r' d\theta, \tag{3.3}$$

$$\dot{M}_{\rm net}(r) \equiv \dot{M}_{\rm in} + \dot{M}_{\rm out}, \tag{3.4}$$

where $\dot{M}_{\rm in}$, $\dot{M}_{\rm out}$, $\dot{M}_{\rm esc}$ and $\dot{M}_{\rm net}$ are the inflow rate, the outflow rate, the escape rate, and the net accretion rate, respectively, and v_r' is defined as $v_r' = v_r$ for $v_r \geq v_{\rm esc}$ and

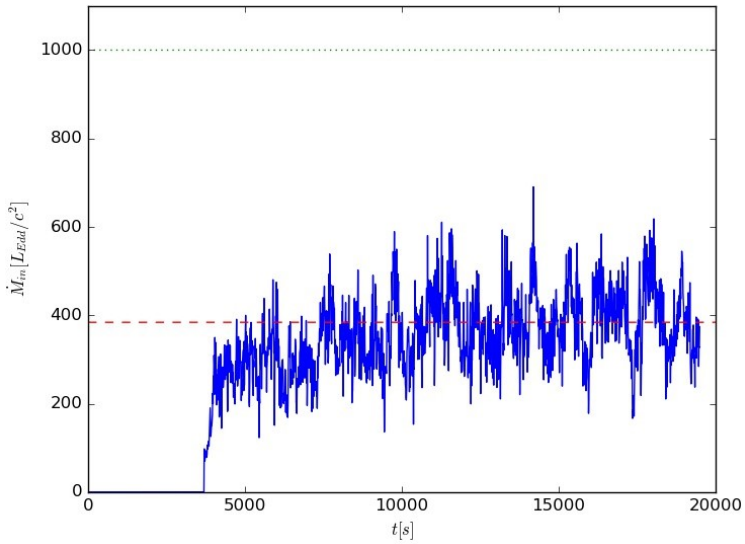

FIGURE 3.1: Time variations of the mass inflow rate onto the black hole ($\dot{M}_{\rm BH}$). The blue line traces the evolution of the inflow matter at the black hole boundary ($r = 2r_{\rm Sch}$). The red dashed line represents the mean value of the blue line but in the quasi-steady state. The green dotted line indicates the mass injection rate at the outer boundary of the simulation box in the inner zone ($r = 3 \times 10^3 r_{\rm Sch}$).

$v'_r = 0$ otherwise. (Note that the BH mass accretion rate corresponds to $\dot{M}_{\rm BH}(t) \equiv |\dot{M}_{\rm in}(r = 2r_{\rm Sch}, t)|$).

In order to plot the integrated mass flux we average the integral over time (instead of integrating the time averages), in accordance to Stone, Pringle, and Begelman (1999). For the quasi-steady state to be completely achieved in a simulation we should see that $\dot{M}_{\rm net} \simeq$ cnst, however this is not realistic (since it would require more than a year of computational time) nor completely necessary. We see, in Figure 3.2, that the net rate presents 2 distinct flow patterns, inside and outside the Keplerian radius. First we show how mass flows at a rate of $\dot{M} \sim 1000(L_{\rm Edd}/c^2)$, which then gets divided in the two flows: inflow ($\sim 400(L_{\rm Edd}/c^2)$), and outflow ($\sim 500(L_{\rm Edd}/c^2)$). While the total simulation has not reached the quasi-steady state (i.e., circulating flow region net flux is not constant), the inflow and outflow regions have ($\dot{M}_{\rm net}(r < 100) \sim$ cnt & $\dot{M}_{\rm net}(r > 1000) \sim$ cnt).

In Figure 3.2 we can also observe that the mass accepted by the BH is only a fraction of the injected mass per time. The remaining part will be circulated or ejected as outflow (see below).

Time averaged inflow-outflow structure in the 1^{st} stage simulation is summarized in the left panels of Figure 3.3: from top to bottom, two-dimensional (2D) distributions of the gas density, the radiation energy density (E_0), and the kinematic energy, respectively. In the upper left panel we see a 'bulge' (or puffed-up) structure, which is created by a small-scale circulation of gas formed between $100r_{\rm Sch} < r < 1000r_{\rm Sch}$ (see Figure 3.4). It is important to note that such an inflated structure is created when the Keplerian radius is relatively small, as was demonstrated by Kitaki et al. (2021). We also observe low-density atmosphere surrounding the bulge structure, although it is not a static atmosphere but is composed of outflow (explained later).

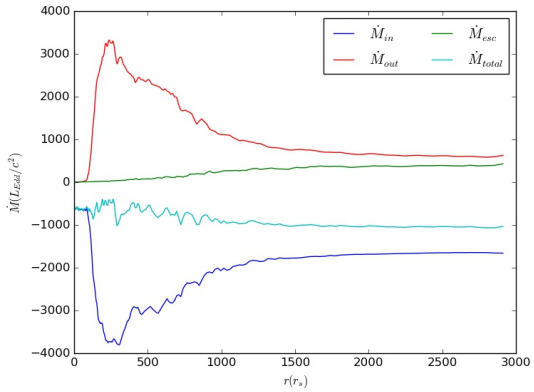

FIGURE 3.2: Radial trend of the mass inflow/outflow rate in the 1^{st} stage simulation. The mass inflow rate ($v(r,\theta) < 0$), the mass outflow rate ($v(r,\theta) > 0$), the escaping mass outflow rate ($v(r,\theta) \geq v_{\rm esc}$) and the net mass flow rate are indicated by the dark blue, green, red, and cyan lines, respectively.

3.2 Outflow structure

Once the gas flow has reached the innermost region, outflow processes begin to produce powerful winds. In this section, we will trace the outflow in the 1^{st} stage simulation.

There exists circulating flow patterns extending close to the outer boundary in the 1^{st} stage simulation, although it is not always visible in the time-averaged plots of Figure 3.3 but we can confirm its presence in Figure 3.2, since a large bump in the $\dot{M}_{\rm out}$ curve and a large hollow in the $\dot{M}_{\rm in}$ curve are formed by the large-scale circulation flow(see also Figure 3.4 for the inner portions of circulating gas flow). It is thus important to note how to choose the outer radius of the 1st stage simulation. If the radius of the outer boundary is chosen to be smaller than the circulating zone, mass will flow out of the simulation box and be lost, leading to an underestimation of $\dot{M}_{\rm BH}$. While a bigger simulation box could contain the larger scale phenomena, we would then be obliged to adopt coarse grid-point spacing to perform simulations within a reasonable time. This would then result in missing details in the flow structure. Considering these facts, we have fixed the outer boundary of the 1st simulation to be at $3000r_{\rm Sch}$.

In the middle left panel of Figure 3.3 we see that the radiation energy density monotonically decreases outward in a nearly spherically symmetric fashion. More precisely, the constant E_0 contours show a bit elongated in the vertical direction, which indicates radiation is going out more dominantly in the vertical (z) direction. The kinetic energy distributions displayed in the lower left panel, by contrast, show somewhat distinct patterns. First of all, the inflow (disk) region is clearly visualized, since not the radial velocity but the rotational (v_ϕ) velocity is dominant and is comparable to the free-fall velocity. Second, outflow region, in which large $E_{\rm kin}$ is found, is rather elongated in the vertical direction. Third, the kinetic energy is at minimum above the disk region at large radii. To summarize, kinetic energy is released predominantly in the perpendicular direction to the disk plane. This feature will further be examined in the next subsection.

We can study the outflow properties near the outer boundary of this inner zone ($r \sim 3000r_{\rm Sch}$), to understand what to expect in the next stage. To do this, we look at the azimuthal profiles of hydro-dynamical variables near the outer boundary (as

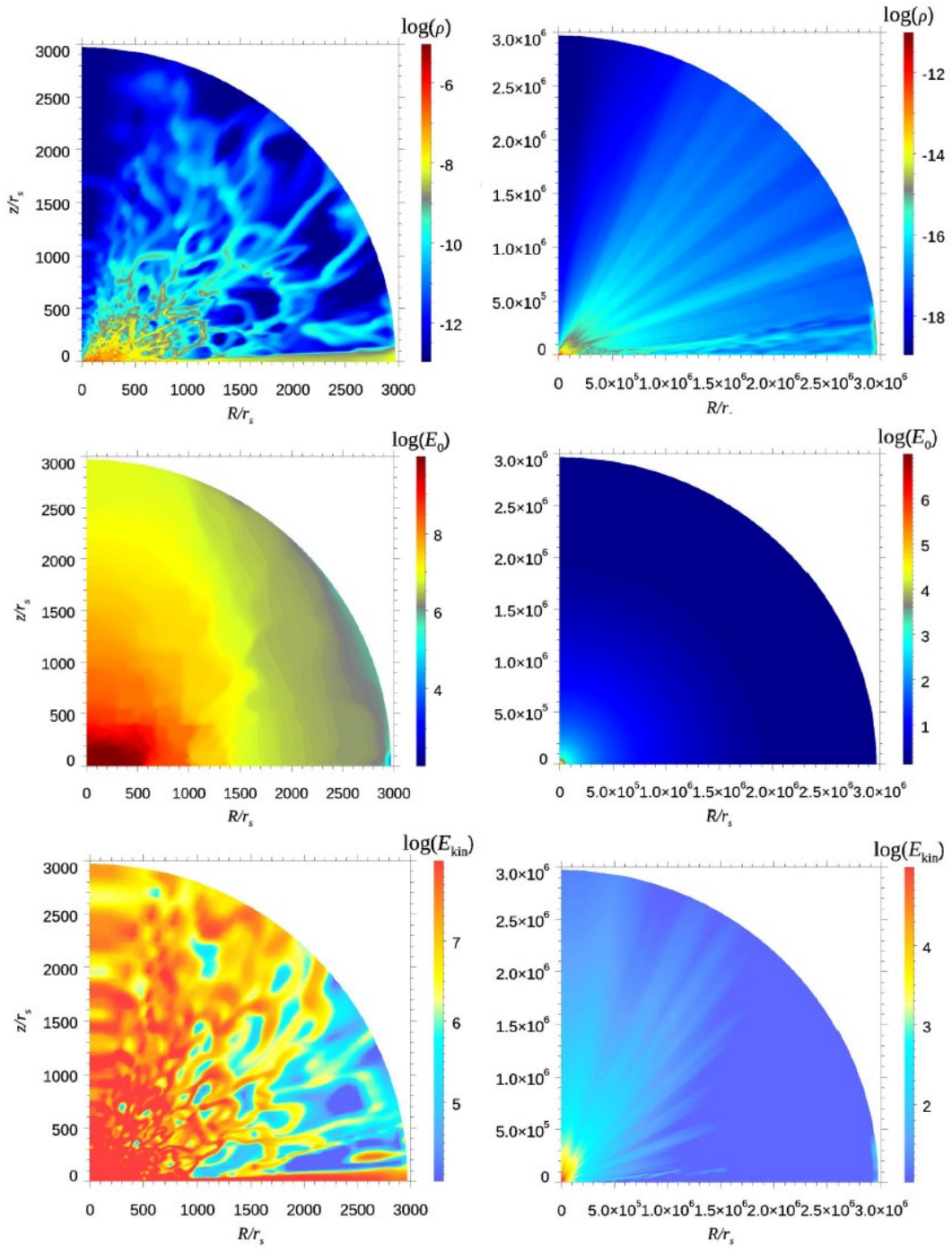

FIGURE 3.3: Two-dimensional (2D) contours of matter density (top), radiation energy density (middle), and kinetic energy density (bottom) in the inner zone (left) and outer zone (right). Note different color bars for the left and right panels; they are adjusted to clearly visualize rapid spatial variations of the physical quantities.

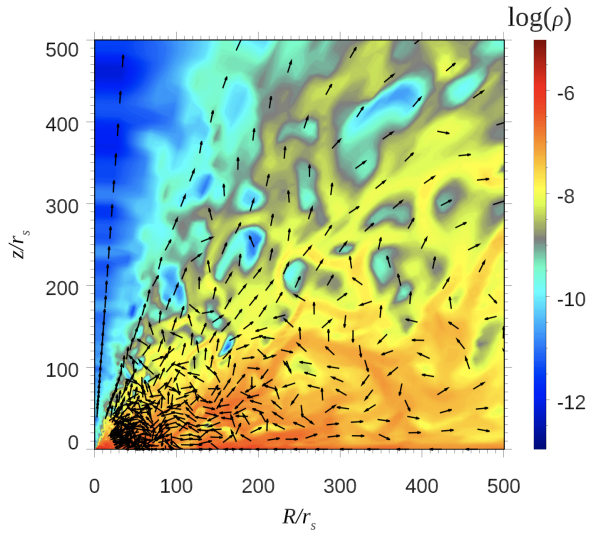

FIGURE 3.4: A typical snapshot of the two-dimensional (2D) contours of matter density in the 1^{st} stage (at $t = 18000\,s$) centered around the 'bulge'. The black arrows show the velocity vector map of each grid point.

shown in Figure 3.5), where we see 3 distinct regions:

- Inflow region ($\theta_{\rm ah} < \theta \leq \pi/2$): high density gas with negative velocity.
- Uncollimated outflow region ($0.4 < \theta < \theta_{\rm ah}$): constant density $\rho \sim 10^{-11}$ g cm^{-3}, non-relativistic velocities ($0.01 < v_r/c < 0.03$).
- Collimated jet region ($\theta < 0.4$): low density gas capable of achieving relativistic velocities ($v_r \sim 0.7c$).

Let us proceed to the 2^{nd} stage simulation to see how outflow propagates further in the outer zone. Let us overview the flow structure, as well as radiation properties, calculated in the 2^{nd} stage simulations in the right panels of Figure 3.3. We see rather smooth distributions of quantities in the right panels. One may thus think that the flow structure and radiation properties in the outer zone could be simple extrapolations of those in the inner zone. It is not precisely the case, however, as will be shown later.

Since we only follow the escaping gas in this stage, we only simulate the outflow structure. This means that, due to the elimination of the inflow region by re-scaling the simulation box on the 2^{nd} stage (see subsection 2.2), all the results and conclusions drawn in this stage will cover only the region at $\theta < \theta_{\rm ah} \sim 1.5$ rad. This value is the limit for which $v_r(\theta) < 0$, as seen in the bottom panel Figure 3.5. In the top panel of the same figure we can confirm that $\theta \sim 1.5$ rad delimits the inflow region from the almost 4 order magnitude drop in density.

In Chapter 2 we discussed the challenges regarding how the program must be adapted and modified for this stage to work. Given these approximations, it is important to showcase the accuracy of our method to connect 2 stages. For this reason, we show some of the physical quantities measured in both of 1^{st} and 2^{nd} simulation boxes at the same radius. Figure 3.6 shows the density profiles, along with radial velocity and radiation energy density, measured in the connection zone shared with the inner and outer zones. This ensures the smooth connections between the two stages.

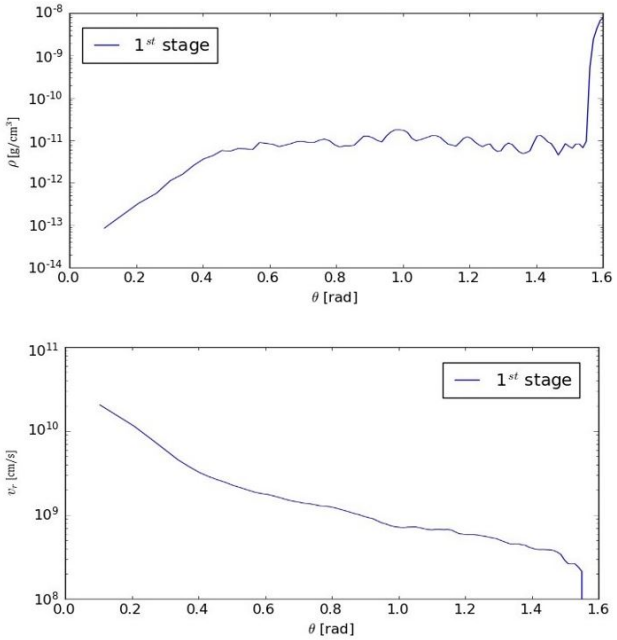

FIGURE 3.5: Density (top) and radial velocity (bottom) angular profiles near the outer boundary of the inner zone. Notice that the radial velocity in the inflow region (i.e., $\theta \sim \pi/2$) diverges due to its negative values.

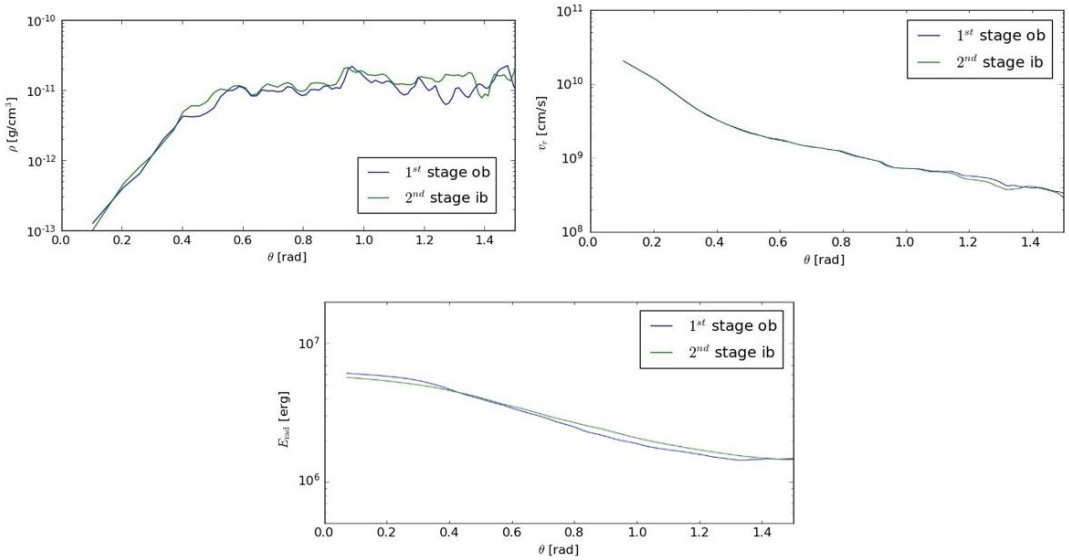

FIGURE 3.6: Angular profiles of the density (top left), the radial velocity (top right) and the radiation energy (bottom) measured at the same radius $r = 2.7 \times 10^3 r_{\rm Sch}$ in the inner zone (blue line) and the outer zone (green line), respectively. This graph showcases the degree of fidelity in which we can reproduce the previous zone result.

In this stage we can also perform a study on the the mechanism of acceleration of wind along the simulation box. For this we can use equation 2.2, which shows that the forces involved in the gas acceleration are: the radiation force (i.e., $\chi/c\, F_{0,r}$), the internal force (i.e., $\partial p/\partial r$), and the centrifugal force (i.e., $\rho(v_\theta^2 + v_\phi^2)/r$). We see in Figure 3.7 that when compared with the gravitational pull, the other forces dominate.

If we break down the contribution we find that the radiation force is responsible for $90 - 99\%$ (from $10^3 - 10^6\, r_{\rm Sch}$) of the push and that the rest comes almost entirely from the centrifugal force.

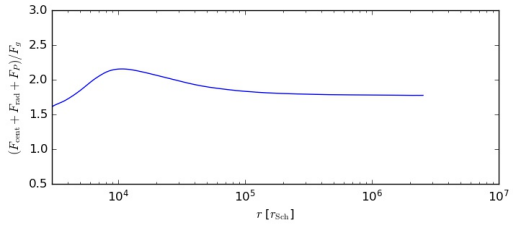

FIGURE 3.7: Force balance between the accelerating forces ($F_{\rm rad}$, $F_{\rm cent}$ and F_p) against the gravitational pull (F_g) in the 2^{nd} stage simulation, averaged over time. We have chosen $\theta \sim 0.87$rad $\sim 50^\circ$ as a representative value of the outflow. This figure demonstrates acceleration of the gas in the outer zone.

We have mentioned that the minimum length scales which cosmological simulations can reach is approximately $r \sim 10^9 r_{\rm Sch}$, whereas our 2^{nd} stage simulation can cover the range up to $r \sim 10^6 r_{\rm Sch}$. Hence there is a gap between them. However, we will demonstrate that the outflow properties can well be extrapolated to even larger radii. This will be attempted in the next subsection.

3.3 Outflow impact

As mentioned in Chapter 1, it is our main objective to provide information regarding what impact the outflow can give to the environmental gas. This is because such impacts are simply assumed or modeled without justification in most cosmological simulations. For this reason, those cosmological simulations tend to miss such an important physical process. But thanks to our nested simulation-box method we can precisely evaluate the mass, momentum, and energy fluxes generated by the outflow winds.

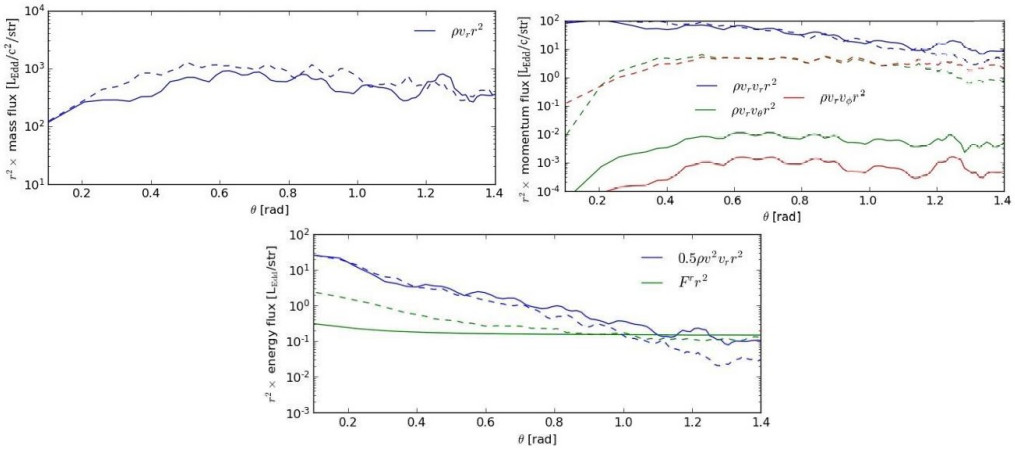

FIGURE 3.8: Linear profiles of mass (top left), momentum (top right) and energy (bottom) flux in the angular direction ($0.0 < \theta < 1.4$). Solid lines indicate the flux at the outer boundary of the 2^{nd} stage (i.e., $r \sim 3 \times 10^6 r_{\rm Sch}$), while the dashed line shows the flux at the outer boundary of the inner zone (i.e., $r \sim 3 \times 10^3 r_{\rm Sch}$).

In Figure 3.8 we show the angular profiles of the mass, momentum, and energy fluxes (all multiplied by r^2) at the outer boundaries of the 1^{st} and 2^{nd} stage simulations. Here we calculate not only the total luminosity but also the isotropic X-ray luminosity and the isotropic mechanical luminosity defined as:

$$L_{\rm X}^{\rm ISO}(\theta) = 4\pi r^2 F^r, \tag{3.5}$$

$$L_{\rm mec}^{\rm ISO}(\theta) = 2\pi r^2 \rho v^2 v_r, \tag{3.6}$$

where $v = \sqrt{v_r^2 + v_\theta^2 + v_\phi^2}$, F^r is the radiation flux in the laboratory frame and we assume that radiation is emitted predominantly in the X-ray band, since the ratio between the X-ray luminosity to the bolometric luminosity is $\sim 71 - 98\%$ from Kitaki et al. (2017) and Narayan, Sądowski, and Soria (2017).

In Figure 3.8 we find that the mass flux profile is nearly flat, but the momentum and energy fluxes tend to grow as the azimuthal angle (θ) decreases (towards the rotation axis). That is, we expect much larger impacts to the environments located in the face-on direction. This is because the gas mass density rapidly decreases (with decreasing θ), while the radial velocity increases. These results are consistent with those of Kitaki+20 (see their Fig. 14).

We have pointed through this paper the importance of moving away from the BH scale to the cosmological scale in order to paint the better picture for the outflow structure. This can be exemplified when comparing the dashed lines with the solid ones in each panel of Figure 3.8. From the top panel, we can understand that if we would study the outflow structure solely in the inner zone (i.e., calculations only in the 1^{st} stage simulation box), we would overestimate its impact by a factor of ~ 2, at most. This is due to the gravitational pull of the central object; that is, the outflow with velocity being less than the escape velocity cannot reach the infinity. This is what we called failed outflow (see section 3.1 discussion).

In the middle panel of Figure 3.8 we can see that radial momentum flux far exceeds the other components. We also find that the θ- and ϕ- momenta decrease outward, but these can be easily understood from the viewpoints of the angular momentum conservation. In fact, they are about 3 orders of magnitude larger in the 1^{st} stage (measured at $3 \times 10^3 r_{\rm Sch}$) than in the 2^{nd} stage (measured at $3 \times 10^6 r_{\rm Sch}$).

In the last panel (bottom), we see how the energy impact is mostly dominated by the mechanical flux, except near the equatorial plane. We can also see how the impact from radiation flux increases towards the rotation axis (with a decrease in θ). At the same time its impact is reduced as we increase the radius, and becomes almost spherically symmetric near $r \sim 3 \times 10^6 r_{\rm Sch}$ (i.e., the radiation flux in the 2^{nd} stage (see the solid green line) has a nearly flat profile and, overall, it is smaller than the same flux in the 1^{st} stage (see the dashed green line)). This radial decrease in the impact caused by the radiation flux predicts a mechanical dominated energy impact at the cosmological boundary ($r \sim 10^{8-9} r_{\rm Sch}$). It is important to point that the mechanical energy flux, in the outer zone, is by over one order of magnitude greater at large θ than that in the inner zone, indicating that it does increase radially as the outflow propagates outward. This is due to the continuous acceleration of outflowing gas by receiving radiation pressure force.

In order to more explicitly demonstrate the acceleration of outflowing gas and the continuous increase of mass outflow rate at small θ we show the radial profile of the gas density, radial velocity, as well as those of mass, momentum, and energy fluxes for fixed angles of $\theta = 0.2$ ($\sim 11^\circ$), 0.8 ($\sim 46^\circ$), and 1.4 ($\sim 80^\circ$) in Figure

3.9. These plots not only demonstrate the smooth connection of physical quantities between the two stage simulations but also show rather uniform structure in the 2^{nd} stage simulation. In this sense, the results of the 2^{nd} simulation can be predicted by those of the 1st simulation, but there is one important exception. That is, the mechanical energy flux (shown in the bottom panel) shows a clear tendency of increase with an increase of radius for the nearly edge-on case (with $\theta = 1.4$). This is the direct evidence of continuous acceleration of outflow travelling in the nearly edge-on direction.

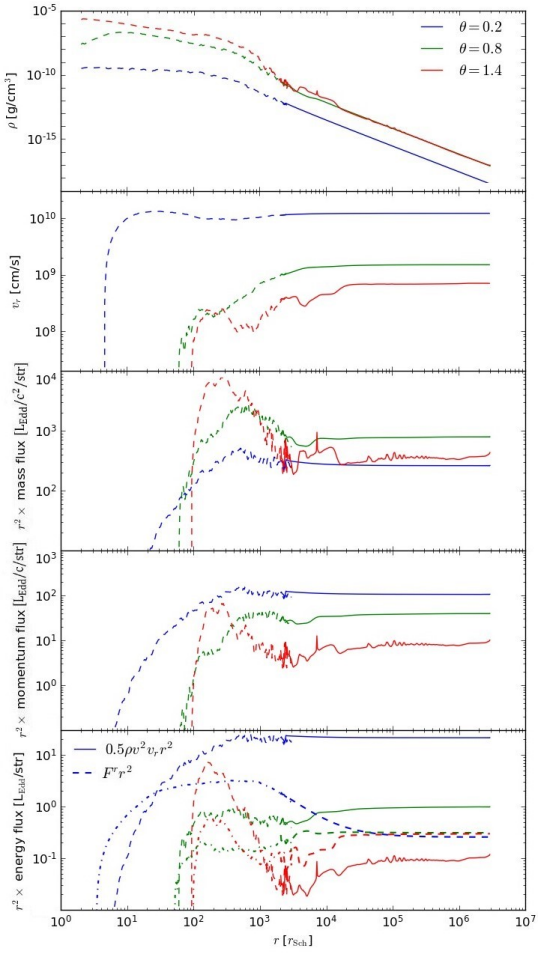

FIGURE 3.9: From top to bottom: Linear profiles of density, radial velocity, radial mass flux ($\rho v_r r^2$), radial momentum flux ($\rho v_r^2 r^2$) and energy flux in the radial direction. Each panel shows both the 1^{st} (dashed) and 2^{nd} (solid) stage lines. The energy flux panel (last) contains also the radiation flux for the 1^{st} and 2^{nd} stages, indicated by a dotted and a dot-dash line respectively.

To accurately establish the impact of the outflow into the outer medium, it is also important to know what the total mass flux is at the outermost boundary (i.e., the outer boundary of the outermost box). If we proceed in a parallel manner as Equation (3.2), we obtain that $\dot{M}_{\rm out}(r = 3 \times 10^6 r_{\rm Sch}) \sim 317.5 L_{\rm Edd}/c^2 \approx 0.3 \dot{M}_{\rm inj}(r = 3 \times 10^3 r_{\rm Sch})$. This implies that from the input material, we are losing 30% of it as outflowing wind.

We can use the 2^{nd} stage data to extrapolate to cosmological scales ($\sim$ 0.1 pc). This is because, inside the computational box in this stage, $\dot{M}_{\rm out} = \dot{M}_{\rm esc}$ is reached at $r \sim 6000 r_{\rm Sch}$, thus the outflow measured at the outer boundary will contain no

failed outflow. The radius at which this condition is met seems to depends on several factors ($\dot{M}_{\rm inj}$, $r_{\rm Kep}$, $M_{\rm BH}$), but we need further studies to specify which factor is most essential. For this we can use the profiles shown in Figure 3.9, where we can see how the density and velocity (first 2 panels) trends become smooth for $r > 10^5 r_{\rm Sch}$. In particular we see how at the larger scales $\rho \propto r^{-2}$ and $v \propto r^0$. Using these trends, we obtain that $\rho(10^9 r_{\rm Sch}) \sim 10^{-23} - 10^{-25}{\rm g/cm^3}$, $v_r(10^9 r_{\rm Sch}) = 3 \times 10^9 - 2 \times 10^{10}{\rm cm\ s^{-1}}$, for $\theta = 0 - 1.5$.

This is particularly important, since it allows us to compare our results with cosmological studies that assume a certain outflow from the central particle (Debuhr, Quataert, and Ma 2012 Dbr+12). In their study they assume a sub-Eddington outflow defined by $v_r \sim 10^4{\rm km\,s^{-1}} = 10^9{\rm cm\,s^{-1}}$, momentum flux $\sim \tau_w L/c$ and energy flux $\sim 0.01\tau_w L$, where $\tau_w = 1 - 10$ and the luminosity $L = \min(0.1\dot{M}_{\rm in}c^2, L_{\rm Edd})$. From Figure 3.9, by contrast, we find momentum flux $\sim 10 - 100 L/c$ and energy flux $\sim 0.1 - 10L$ (where our luminosity is obtained from the last panel of Figure 3.8 as $L \sim 0.25 L_{\rm Edd}$) with stronger impacts produced towards the nearly face-on direction than in the nearly edge-on direction. Our model predicts in overall stronger impacts on the environments, with a similar radial speed (i.e., $v_r \sim 10^9{\rm cms^{-1}}$) and energy to momentum flux relation (i.e., energy flux about 100 times smaller than momentum flux) for $0.7 < \theta < 1.5$, for the super-Eddington accretion scenario. The presence of a stronger wind in our model is expected from our super-Eddington scenario (which is effective when the black hole mass is relatively small) when compared to sub-Eddington scenarios, but our model can account for the presence of a collimated relativistic jet, which produces a bigger impact in the azimuthal direction. This anisotropy in the velocity is not found in wind models in other studies.

3.4 Discussion

With the analysis of the results completed, we can proceed to discuss the implications of these accretion rate, outflow profile and its impact. Before that, we need to mention the importance that the NSB method had in producing this simulation.

3.4.1 Benefits of the NSB method

In Chapter 1, we presented the shortcomings of both cosmological and astrophysical simulations. We remarked the difficulty in solving the bridge between them due to enormous computational times. In our project the inner zone (i.e., $2r_{\rm Sch} < r < 3000 r_{\rm Sch}$) took approximately 3 weeks to simulate for the lower angular momentum models. The simulation time increases drastically with the Keplerian radius, which at the time of writing this thesis has taken around 5 months without reaching the quasi-steady state.

Increasing the radius of the outer boundary by an order of magnitude, while keeping the inner boundary position and the number of grid points constant, would make the simulation cost increase enormously. Not to mention that if we would increase the radius of the outer boundary, while keeping the same grid point number, we would also be losing resolution in the smaller scale. This would result in a grid size incapable of resolving correctly the circulating structure thus being incapable of correctly accounting for outflow or inflow values. Which would mean that for example, we would not be able to see the filamentary structure of the outflow, nor being able to see the distinction of the wind generation mechanisms between models. The only way to overcome this would be to increase the grid point density together with

the outer boundary which would increase the computational time too much, making it unfeasible.

By using the Nested Simulation-Box method, by contrast, we can save time. In fact, the 2^{nd} stage (i.e., $2000r_{\rm Sch} < r < 3 \times 10^6 r_{\rm Sch}$) took only 5 days or so. In total the simulation cost of by using our method allowed us to reduce an impossibly long simulation to simply one month, for the low angular momentum models.

By using our NSB method in different models we have demonstrated that beyond fast it is also a consistent method. We saw prove of that in subsections 3.3, where the smooth connection between hydro and radiation variables was done smoothly outside the connection area, where we no longer impose the values (see Figures 3.6). This represents a very important step towards creating more realistic models of galaxy evolution, in particular in the early universe where visual information is scarce as we previously discussed.

3.4.2 Inflow rate comparison

Using the results we obtained from Figures 3.1, we find that, our model predicts a mass growth of $\dot{M}_{\rm BH} \sim 0.4\dot{M}_{\rm inj}$ for this higher injection rate models. By studying the $\dot{M}_{\rm out}/\dot{M}_{\rm BH}$ ratio and comparing our results with those by past studies (see a Table 5.1). We can see that, for this 1^{st} model, the outflow rate over the accreted flux ratio is only larger than the case studied in Kitaki et al. (2021). This fits with what we have explained of models with low Keplerian radius under super-Eddington flow.

The behaviour of this 1^{st} model is explained due to the low-angular momentum with high accretion rate, which generate a very powerful wind but somewhat unrealistic. By comparison in Kitaki et al. (2021) where we see higher angular momentum models they obtain a lower percentage of the mass being expelled by the central object.

3.4.3 Outflow structure and impact relevance

Besides the inflow study, our method, as we showed, also allowed us to trace the jet and outflow structure of such bodies. Powerful outflow, if exists, would collide with inflow gas stream, thereby being able to suppress the gas inflow motion. Such effects were not properly considered in the cosmological simulation (e.g. Shlosman et al. 2016). In fact, these studies either do not include AGN feedback or adopt just a simplistic model. The extension of the outflow effects on such scales is dependent on the pressure exercised by the accretion structure.

We have explained how we can extrapolate our results to higher scales, in particular at a radius ~ 0.1 pc. The relevance of being capable of doing this extrapolation was to compare our results with more simplistic wind models used in other projects (e.g., Dbr+12). If we compare the magnitude of the impact generated by the wind produced in our models we can see that for the 1^{st} model the impact is lager by a factor of around $\times 10$. When we reduced the injection rate (i.e., 2^{nd} model), we see that the wind power is reduced and the impact is $\times$... the one assumed in Dbr+12.

This difference stems from much larger velocities and highly anisotropic velocity profile (see the middle panel in Figure 3.6), whereas they assumed the spherical symmetric non-relativistic velocity profile. From Dbr+12 we see that momentum fluxes $\gtrsim 3L/c$ are expected to produce AGN-driven galactic outflows capable of suppressing star formation and accretion in the host galaxy. Given the results obtained in our model, where momentum flux $10 - 100L/c$, we expect a larger impact of the global interstellar gas, than that assumed in cosmological simulations.

It is relevant to note that larger velocities in the present simulation may be due to small $r_{\rm Kep} = 100 r_{\rm Sch}$, which may lead to larger outflow rates (see discussion in Kitaki et al. (2021), where they assumed relatively large Keplerian radius (i.e., large angular momentum of the injected gas), and find no puffed-up structure and significantly smaller mass outflow rate). We are currently performing a larger keplerian angular simulation to confirm this results.

Chapter 4

Reduced injection model

We can now apply the NSB method to the case with lower injected rate (i.e., $\dot{M}_{\rm inj} = 500\, L_{\rm Edd}/c^2$). By simulating this model we want to better understand a few factors: How does $\dot{M}_{\rm BH}$ change with the injected rate, how does the outflow impact change, and how does the outflow profile change.

For an easier comparison we will proceed on a parallel manner to the 1^{st} model, that is starting at the inner simulation box, extending the outflow to the outer box, and then extrapolating the results to the cosmological boundary.

4.1 Inflow

Just as before, due to the low value of the Keplerian radius, the gas evolves freely until it reaches the $100 r_{\rm Sch}$ mark.

By using the mass flux equations presented in the previous section (i.e., Equations 3.1-3.4), we can study whether the quasi-steady state has been reached.

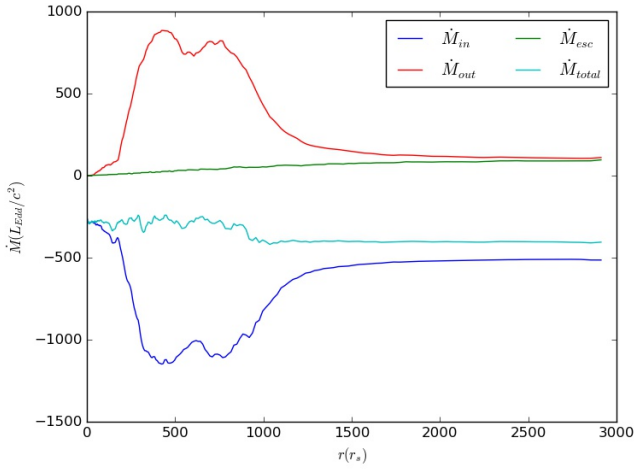

FIGURE 4.1: Radial trend of the mass inflow/outflow rate in the 1^{st} stage simulation. The mass inflow rate ($v(r,\theta) < 0$), the mass outflow rate ($v(r,\theta) > 0$), the escaping mass outflow rate ($v(r,\theta) \geq v_{\rm esc}$) and the net mass flow rate are indicated by the dark blue, green, red, and cyan lines, respectively.

We can see in Figure 4.1, that both inside the Keplerian radius and in the outflow region $\dot{M}_{\rm net}$ is mostly constant. This as before is enough for us to study the inflow and outflow properties. Before that, we can compare this figure with Figure 3.2, where we see that the circulating flow or "bulge" is larger. Not only that we can see that in the reduced inject model, there is almost no failed outflow outflow at the outer boundary.

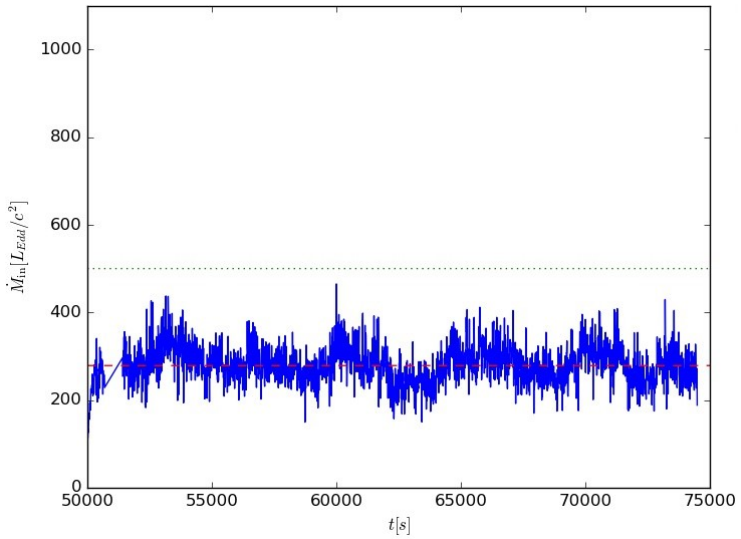

FIGURE 4.2: Time variations of the mass inflow rate onto the black hole ($\dot{M}_{\rm BH}$). The blue line traces the evolution of the inflow matter at the black hole boundary ($r = 2r_{\rm Sch}$). The red dashed line represents the mean value of the blue line but in the quasi-steady state. The green dotted line indicates the mass injection rate at the outer boundary of the simulation box in the inner zone ($r = 3 \times 10^3 r_{\rm Sch}$).

Just as before we can check in Figure 4.2 the accretion rate at the boundary of the central object. We see that the accreted mass flux presents some fluctuations around a constant value ($\dot{M}_{\rm BH} = 282.1\ L_{\rm Edd}/c^2$). This means that a bit less than 60% of the injected gas is being accreted into the central object. This is a significant increase compared to our previous simulated case, where less than 40% of the total injected mass was successfully accreted.

4.2 Outflow structure

As we have seen in the previous case, once the gas falls on the BH we have can distinguish 2 types of structure: the "bulge" and the outflow. We can see these components of the structure clearly in Figure 4.3.

Some important differences to notice is that the over-dense circulating flow is similar in size when compared to the higher injection rate model, but the long range circulation is extinguished much faster. This similar accumulation of matter around the central particle helps us understand the difference in inflow and outflow flux between models. Because the mass acceptance rate of the BH is below the injected rate, an over-accumulation of material forms in either model, allowing the accretion rate to be maximized. On the other hand, because the lower input the gas that formed the outflow previously is considerably reduced.

This reduction of the outflow can be confirmed in the bottom left panel of Figure 4.3, where previously we could not distinguish outflow coming from the collimated azimuthal direction, and dragged outflow from the circulating flow (see bottom left panel of Figure 3.3). But in the lower injection model we can clearly see that the outflow component that has been severely reduced is the one coming from the "bulge".

Lastly if we take a look at the middle panels, we can see that the radiation energy (E_0) presents a very similar profile in the inner zone, when compare to the higher injection rate model. The radiation energy similar to the hydro-dynamic variables

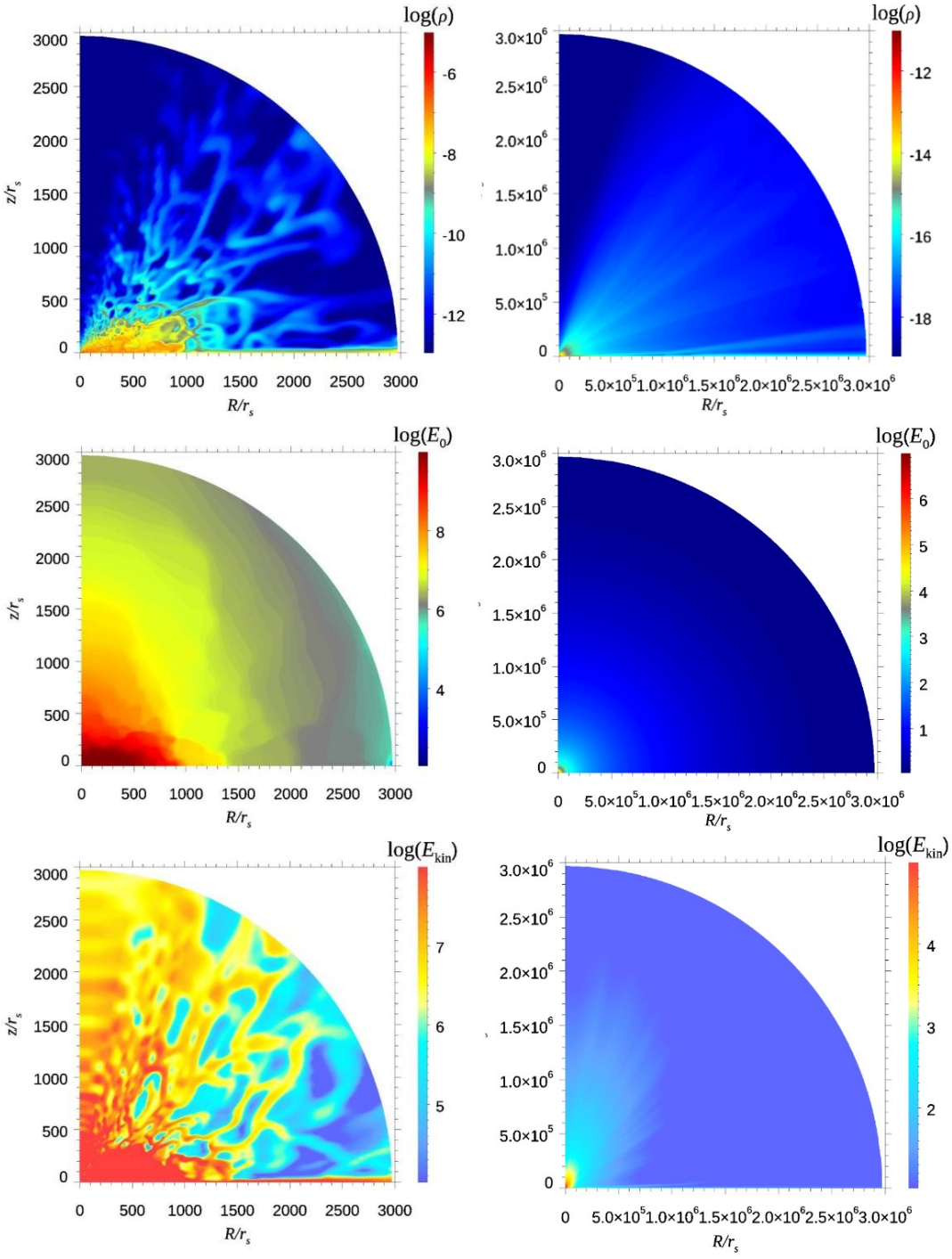

FIGURE 4.3: Two-dimensional (2D) contours of matter density (top), radiation energy density (middle), and kinetic energy density (bottom) in the inner zone (left) and outer zone (right). Note different color bars for the left and right panels; they are adjusted to clearly visualize rapid spatial variations of the physical quantities.

also presents an overall smaller value for the outflow region specially noticeable in the azimuthal direction. In this case it translates to a profile closer to spherically symmetric than what we saw in the inner zone of the previous case studied.

Now the last thing to do in this 1^{st} stage to better understand the properties of the outflow flux is to look at the θ-profiles of the hydro-dynamical variables of the wind near the end of the simulation box.

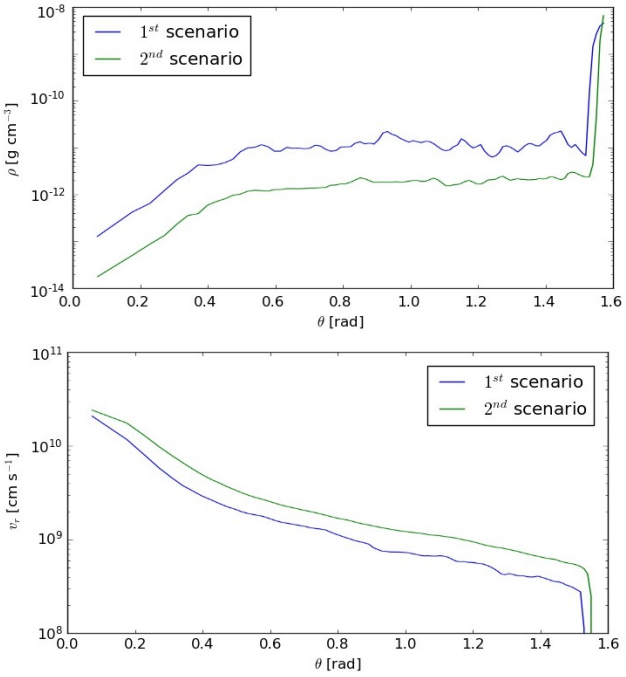

FIGURE 4.4: Density (top) and radial velocity (bottom) angular profiles near the outer boundary of the inner zone. Notice that the radial velocity in the inflow region (i.e., $\theta \sim \pi/2$) diverges due to its negative values.

We can see from Figure 4.4 that our preliminary analysis of the outflow winds was correct. In particular we see a drop of almost an order of magnitude in both the uncollimated outflow region (i.e., $0.4 < \theta < \theta_{\rm ah}$) and the collimated region (i.e., $\theta < 0.4$) of the density. In the radial velocity plot, we can see how the wind speed near the inflow region (i.e., negative velocity region) has increased compared to the higher injection case. The rest of the profile smoothly converges to the previous model at $\theta \sim 0$. This lower density curve, but higher velocity profile behaviour shows that this model indeed produced weaker outflow flux but with less failed outflow included.

We would be remiss if we would not subject this model under the same scrutiny as before. We need to prove the consistency of our NSB method, and we can do that by comparing the density, radial velocity and radiation energy profile between both simulation boxes. We perform the same analysis as before, by showing each variables angular profile in the shared area between simulation boxes, but outside the control area (i.e., area where variable values are imposed, see Chapter 2 for in-depth explanation).

4.3 Outflow impact

The last thing we have to do in this section is to check and analyze the impact that this lower injection model presents at the outer boundary of its outermost stage.

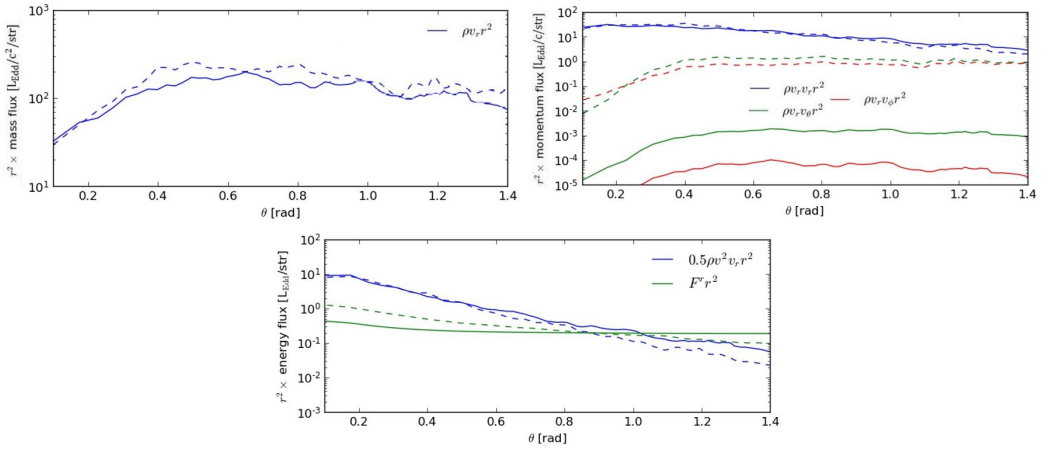

FIGURE 4.5: Linear profiles of mass (top left), momentum (top right) and energy (bottom) flux in the angular direction ($0.0 < \theta < 1.4$). Solid lines indicate the flux at the outer boundary of the 2^{nd} stage (i.e., $r \sim 3 \times 10^6 r_{\rm Sch}$), while the dashed line shows the flux at the outer boundary of the inner zone (i.e., $r \sim 3 \times 10^3 r_{\rm Sch}$).

Same as before we will see in Figure 4.5, how the mass, momentum and energy fluxes angular profiles behave. Note that in each panel, the solid lines belong to the flux measured at the outer boundary of the 2^{nd} stage and the dashed ones belong to the 1^{st} stage.

Starting our analysis on the mass flux panel, we see a very similar profile as we did in the higher injection case. That is, a nearly flat line, that presents a decay on the area belonging to the relativistic wind (i.e., $\theta > 0.4$). The main difference comes in the magnitude of the flux, when compared to the previous model we see that in this case the mass flux has been reduced by almost and order of magnitude. This is consistent with the results from the density profile of the wind which showed a similar decrease.

The second pane, the momentum flux profiles, presents an almost identical behaviour as the previous model with only two different features. The first and less impactful is that the angular momentum flux profiles present a smaller decrease with θ. This implies that when the wind power decreases, the relativistic jet region of the outflow carries more of the angular momentum from the disk than its stronger counterpart. This, while being an interesting feature, is not crucial to the study of the wind at higher scales due to the fast loss of momentum with the radius (see section 3.3 for the discussion on this decay). The other difference between models is found in the r-component of the momentum, where we have the decrease in intensity that we also saw in the mass flux panel.

Lastly we need to talk about the energy flux. As was the case for the rest of the panels we do not see any remarkable changes in this panel either. We see that the radiation energy profile of the 1^{st} simulation box was slightly lower than in the previous model and the same for the mechanical flux. And that in the 2^{nd} simulation box, the profiles match those of the higher injection case, but with a smaller impact in the case of the gas energy.

The last important thing to talk about all these plots is how the dashed and solid blue lines (i.e., mass flux, r-momentum flux, mechanical energy flux) are closer than those we saw in the last model. This points again to the concept that under lower injection rate the wind is less capable of dragging material from the bulge creating what we called "failed outflow". Because of the lower percentage of outflow being failed in this case, the density and radial velocity profiles between boxes are closer, thus their flux counterparts also show the same trends.

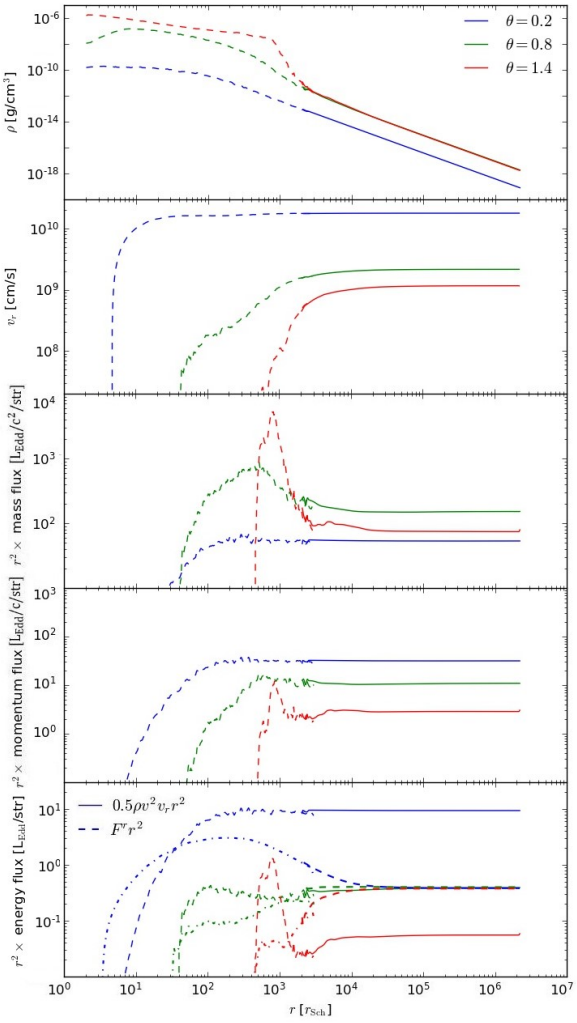

FIGURE 4.6: From top to bottom: Linear profiles of density, radial velocity, radial mass flux ($\rho v_r r^2$), radial momentum flux ($\rho v_r^2 r^2$) and energy flux in the radial direction. Each panel shows both the 1^{st} (dashed) and 2^{nd} (solid) stage lines. The energy flux panel (last) contains also the radiation flux for the 1^{st} and 2^{nd} stages, indicated by a dotted and a dot-dash line respectively.

With the flux impact at the outer stage analyzed we only have a couple thing left to check in this model. One is to confirm that even for this lower impact wind, the 2 stage simulation was needed. We can check this like before, i.e., by studying the different variables (ρ, v_r, mass, momentum & energy fluxes) behaviour over the total length of both simulation boxes together. We perform this study as we did previously in Figure 4.6. Once again we can see just how precise the connection between stages is, thus confirming the validity and strength of out NSB method. We also see once again how most of the variables continue, in the outer simulation box

(solid lines), the trends that presented in the inner zone. With the exception being the variables near the equatorial plane (red lines).

We can also better calculate now the integrated mass flux at the outermost boundary. This will tell us how much of the injected mass leaves the simulation in the form of escaping wind. By using Equation (3.2) on the first panel of Figure 4.5, we get that $\dot{M}_{\rm out}(r = 3 \times 10^6 r_{\rm Sch}) \sim 104.3 L_{\rm Edd}/c^2 \sim 0.21 \dot{M}_{\rm inj}$. For comparison, in the higher injection rate we got that the total escaped outflow at the outermost boundary was $\sim 30\%$.

We now arrive to the last part of the analysis of this simulation, that is extrapolating the results until the inner boundary of cosmological simulations. To do this we use the tendencies shown in Figure 4.6. Following the almost linear trends of density and velocity, seen in the first 2 panels, we obtain that $\rho(10^9 r_{\rm Sch}) \sim 10^{-24} - 10^{-25} {\rm g/cm^3}$, $v_r(10^9 r_{\rm Sch}) \sim 10^9 - 2 \times 10^{10} {\rm cm\ s^{-1}}$, for $\theta = 0 - 1.5$. The values are similar to what we obtained before with slightly lower values in both density and velocity as we already have discussed. The important thing is that now the uncollimated flux velocity is closer to the one presented in Dbr+12. This will allow us to closer compare the values of the impact with those found in their study. We see in fact, in this case our momentum and energy flux are $\sim 1 - 10 L_{\rm Edd}/c^2$ and $\sim 0.01 - 10 L_{\rm Edd}/c^2$. This is very significant for 2 reasons, first we see that now our momentum flux matches the one proposed in Dbr+12. Which shows that the assumed increase in flux is due to the anisotropic profile of the velocity, and it does not need to be imposed. The second is that the energy profile while similar in the edge-on direction, it is 10 times larger in the face-on direction.

There is one last important thing to point out in this impact discussion. That is, that in Dbr+12 they never mention where the energy impact comes from. Since they do hydro-only simulations, in the previous model we used only the mechanical energy flux impact as point of comparison. This was in part because it was overall larger than the one presented in the cosmological study, thus a distinction between mechanical and radiation was redundant. That is no longer the case in this model. The reason is because while it may seem like the impact of the energy flux on the edge-on direction is similar this is only if we do not take into consideration the radiation energy. If we now calculate the energy flux by using the $\max(L_{\rm mec}, L_X)$ we obtain $\sim 0.1 - 10 L_{\rm Edd}/c^2$. This is important because now we get a similar θ dependency, but 10 times as large overall. This shows that by adding the impact of radiation into our study, even when the wind speeds are comparable, and the momentum flux impact is similar, our energy flux impact around an order of magnitude larger.

4.4 Discussion

As was the case for the previous model presented, we will use this last section to summarize the analysis and discuss the repercussion of our results. Since we previously discussed in extend the benefits that the NSB method provided to the study, we will be much more brief. Once more the NSB method allowed us to calculate a simulation box of more than 6 orders of magnitude in roughly a month. Which is not surprising given that between the models the only difference is the injection rate, we expected the same simulation cost.

4.4.1 Inflow rate comparison

In this new scenario we see that the accretion efficiency has risen from the $\dot{M}_{\rm BH} \sim 0.4\dot{M}_{\rm inj}$ that we had in the previous model to $\dot{M}_{\rm BH} \sim 0.6\dot{M}_{\rm inj}$. Not only that but if we also compare the $\dot{M}_{\rm out}/\dot{M}_{\rm BH}$ ratio, in this model the flux rate presents an inverse trend to that seen in the other cases studied where $\dot{M}_{\rm BH}$ is larger than $\dot{M}_{\rm out}$. By comparing the values of accretion rate and outflow rate to the once obtained in the 1^{st} model, we see that reducing the injection rate modifies the outflow rate twice as much as the accretion rate.

This behaviour is most interesting, since it shows that by reducing the inflow rate, we have increased the accretion efficiency (not the accretion rate) and reduced significantly the outflow power. This lower outflow will in return cause less disruption in the medium, thus resulting is a much more efficient BH growth.

By studying these different simulated models we can agree that an accretion efficiency rate of 100% mass growth, which most cosmological simulations assume, is still overestimated. Thus, any conclusion on the capability of raising a super sized SMBHs, produced by those studies, is circumstantial. It is important to note that higher accretion rates still could be feasible, if RHD simulations would include some relativistic accretion mechanisms (e.g. the Blandford-Znajek process Konoplya, Kunz, and Zhidenko (2021)).

We have also had to modify the opacity function at large scales to include the recombination of hydrogen at low temperatures. We used a simplified formulation to include this factor when temperature drops below $T < 10^4 K$. This needs to be included since, as seen in Takeo et al. (2018), the impact of the gas chemistry in the medium is non-negligible.

4.4.2 Outflow structure and impact relevance

Regarding the outflow an its impact on the cosmological scale, we can do a parallel discussion to the one done in the previous Chapter. In this lower injection rate model, which is closer to the sub-Eddington assumption of Dbr+12, we obtained a similar but weaker outflow. We can see that the velocity is still highly anisotropic, but the values at the equatorial plane (i.e., edge-on direction) is now much similar to the one assumed in their study.

The weaker wind generated in this case leads to a momentum flux impact that is comparable to the one assumed in the cosmological simulations, thus showing that the anisotropy in the flux appears naturally due to the similar behaviour in the velocity. However, this is not the case for the energy flux, which is higher than the one considered in their study. In particular we see that the mechanical component of the energy flux is comparable to the one in Dbr+12 around the equatorial plane (uncollimated outflow, means lower velocities). Yet this is not the case when we move towards the azimuthal direction, finding an almost 10 fold difference between our model and theirs. What is more, since our simulation include radiation feedback, we see that in the equatorial plane the radiation component is stronger than the mechanical one. This means that the total energy flux in our model, is overall larger than the one assumed in the cosmological simulations(see Figure 4.6). This is particularly interesting because of the fact that without the radiation component, we would have a very similar feedback profile.

4.5 Future work

Lastly, we are currently performing a third simulation by increasing the angular momentum of the infalling gas, as we pointed in Table 2.2. Although the simulation has not reached the quasi-steady state, thus we can not do a proper outflow discussion, we can add some of the preliminary infall results here. In the first stage, the injected gas from the outer boundary rapidly establishes an unstable orbit at the region around the Keplerian radius, $r_{\rm Kep} = 1000\, r_{\rm Sch}$. Once there it slowly forms a circulating structure that expands until $r \sim 1500 r_{\rm Sch}$ (see Figure 4.7). This structure is slowly pulled by the central object, the inflow and outflow before the bulging structure reaches the AGN is negligible. Once the gas reaches the center we see a similar viscous (slow) accretion process that we saw in the 1^{st} model.

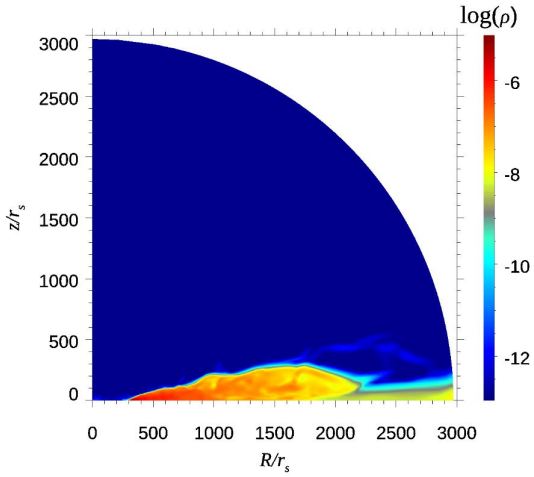

FIGURE 4.7: Two-dimensional (2D) contour of the mass density in the inner zone. The high-angular momentum gas forms a circulating structure ("bulge") far from the central object.

As we stated, the inflow takes much longer to initiate in this case ($t_{\rm acc} \sim 8 \times 10^4$ s). Once it starts we see an initial peak due to the accumulation of mass at the edge of the circulating structure. This is quickly settled and, while the mass flux fluctuates over time like before, we see that its average settles down in a constant value $\dot{M}_{\rm BH} = 412 L_{\rm Edd}/c^2$.

In future, we wish to continue improving the Nested Simulation-Box method. As previously mentioned, our method was applied to a simplified case as a framework to develop and test our methodology. We certainly need extensive parameter studies to clarify the dependences of the results on several parameters, such as the alpha parameter and the Keplerian radius. It will also be interesting to vary BH mass, keeping the mass injection rate, since the outflow properties may possibly depend on the Eddington ratio; i.e., weaker impacts may arise in the sub-Eddington regime. There is also the need to incorporate the general relativistic (GR) effects, as well as to analyze and develop a better physics environment for the even larger simulation box. Specifically, we wish to introduce a better approach to the energy diffusion due to b-f collisions when the gas passes the ionized temperature threshold.

Chapter 5

Conclusions

We started this study by introducing the extreme difficulty of performing a thorough study the gas dynamics around the high redshift AGN. In particular we focused on the disconnection between the studies of these objects in BH astrophysics and cosmology. Through the implementation of the Nested Simulation-Box method we have managed to bridge that gap. In this method we first calculate inflow-outflow structure in the inner zone and follow the outflow propagation in the outer zone with smooth connection between them. The nested simulation-box method allows us to follow the evolution of outflow structure in a self-consistent fashion from astronomical scale to cosmological scale, while maximizing the computational efficiency. We used the NSB method on two different models which we can compare with other similar studies:

Method Study	Compton [Yes/No]	$r_{\rm out}$ $[r_{\rm Sch}]$	$r_{\rm Kep}$ $[r_{\rm Sch}]$	$\dot{M}_{\rm BH}$ $[L_{\rm Edd}/c^2]$	$\dot{M}_{\rm out}$ $[L_{\rm Edd}/c^2]$
Newtonian-2D					
Ohsuga+11	No	105	40	~ 100	
Kitaki+21	Yes	300	2430	~ 180	~ 24
Ohsuga+05	No	500	100	~ 130	
Kitaki+18	Yes	3000	300	~ 280	~ 300
Hashizume+15	No	5000	100	~ 150	~ 500
Botella+22	Yes	3×10^6	100	~ 380	~ 320
Reduced Ingection	Yes	3×10^6	100	~ 280	~ 100
Newtonian-3D					
Jiang+19	Yes	800	40	~ 250	
GR-2D					
Sądowski+15	Yes	2500	21	~ 420	~ 7000
GR-3D					
Jiang+14	No	50	25	~ 220	~ 400
Takahashi+16	No	125	17	~ 200	
Sądowski+16	Yes	500	20	~ 180	~ 520

TABLE 5.1: Comparison between results form different studies using RHD & RMHD simulations. Here we compare the box size ($r_{\rm out}$), the angular momentum of the injected material ($r_{\rm Kep}$), and the mass flux both at the BH boundary ($\dot{M}_{\rm BH}$) and at the outer boundary ($\dot{M}_{\rm out}$). We also indicated whether the Compton scattering effect is taken into account or not.

After our thorough analysis of these models what we find with this method, can be summarized as follows:

- Under an inflow rate of $\dot{M} = 10^3 L_{\rm Edd}/c^2$, the accretion rate onto the central object is $\dot{M}_{\rm BH} \sim 0.4\dot{M}_{\rm inj}$ (see Figure 3.1). That is, about 60% of gas is lost as outflow.
- When lowering the inflow rate to $\dot{M} = 500 L_{\rm Edd}/c^2$, the accretion rate onto the central object becomes $\dot{M}_{\rm BH} \sim 0.6\dot{M}_{\rm inj}$ (see Figure 3.1). Showing that under lower injection rates the system becomes more efficient (i.e., lower percentage of infalling mater is lost as outflow)
- We confirm the presence of failed outflow, which is launched at smaller radii but falls back to the disk at larger radii (top and bottom panels of Figure 3.3). Due to the presence of such a large-scale circulating flow we need to take sufficiently large simulation box in the inner zone. This component of the wind is less prevalent when the injected flux is reduced.
- Outflow structure is much simpler in the outer zone and can be extrapolated beyond the outmost boundary of our simulation ($r \sim 10^6 r_{\rm Sch}$) (see Figure 3.3). The possible impacts of the outflow on the cosmological scale are demonstrated in Figures 3.8 & 4.5.
- Simple extrapolations of the physical quantities calculated in the inner zone do not work (see Figures 3.9 & 4.6).
- For the fiducial model we find an anisotropic near relativistic outflow with density of $10^{-17} - 10^{-19}$ [g cm^{-3}] and velocities of $0.02 - 0.7\ c$. With the lower densities and higher velocities belonging to the azimuthal jet.
- The momentum (energy) impact expected on the cosmological scale (~ 0.1 pc) from the wind from the fiducial model is $\sim 10 - 100 L_{\rm Edd}/c$ ($\sim 0.1 - 10 L_{\rm Edd}$). This is around 10 times larger than those assumed in the cosmological simulation studies (as discussed in Chapter 4), all be it under our large super-Eddington accretion rate.
- The wind impact when the injection rate is reduced is comparable to that seen in cosmological studies, but still highly anisotropic $\rho \sim 10^{-18} - 10^{-19}$ [g cm^{-3}] and $v_r \sim 0.03 - 0.7\ c$.
- In this second model the momentum flux is now comparable with the studies mentioned previously (i.e., $\sim 1 - 10 L_{\rm Edd}/c$). When we compare the different components of the energy flux impact, we see that the mechanical energy flux is also closer, $\sim 0.01 - 10 L_{\rm Edd}$. But when we also account for the presence of radiation our model presents once more a higher value, $\sim 0.1 - 10 L_{\rm Edd}$ (see bottom panel of Figure 4.6).
- In this work we applied our method to two accretion models. But in order to draw a clearer picture of accretion rates and AGN feedback profiles we need to conduct studies with other parameters. We are currently in the process of performing a simulation with a higher angular momentum.
- In order to make it easier to develop, we used some approximations that will be improved in future work. More extensive parameter studies remain to be performed.

Bibliography

Alexander, Tal and Priyamvada Natarajan (Sept. 2014). "Rapid growth of seed black holes in the early universe by supra-exponential accretion". In: *Science* 345.6202, pp. 1330–1333. DOI: 10.1126/science.1251053. arXiv: 1408.1718 [astro-ph.GA].

Bañados, E. et al. (Nov. 2016). "The Pan-STARRS1 Distant z > 5.6 Quasar Survey: More than 100 Quasars within the First Gyr of the Universe". In: *ApJs* 227.1, 11, p. 11. DOI: 10.3847/0067-0049/227/1/11. arXiv: 1608.03279 [astro-ph.GA].

Bañados, Eduardo et al. (Jan. 2018). "An 800-million-solar-mass black hole in a significantly neutral Universe at a redshift of 7.5". In: *Nature* 553.7689, pp. 473–476. DOI: 10.1038/nature25180. arXiv: 1712.01860 [astro-ph.GA].

Begelman, Mitchell C. (Feb. 2010). "Evolution of supermassive stars as a pathway to black hole formation". In: *MNRAS* 402.1, pp. 673–681. DOI: 10.1111/j.1365-2966.2009.15916.x. arXiv: 0910.4398 [astro-ph.CO].

Begelman, Mitchell C., Marta Volonteri, and Martin J. Rees (July 2006). "Formation of supermassive black holes by direct collapse in pre-galactic haloes". In: *MNRAS* 370.1, pp. 289–298. DOI: 10.1111/j.1365-2966.2006.10467.x. arXiv: astro-ph/0602363 [astro-ph].

Booth, C. M. and Joop Schaye (Dec. 2009). "Simulations of the Growth of Black Holes and Feedback from Active Galactic Nuclei". In: *The Monster's Fiery Breath: Feedback in Galaxies, Groups, and Clusters*. Ed. by Sebastian Heinz and Eric Wilcots. Vol. 1201. American Institute of Physics Conference Series, pp. 21–24. DOI: 10.1063/1.3293041.

Brightman, Murray et al. (May 2019). "Breaking the limit: Super-Eddington accretion onto black holes and neutron stars". In: *BAAS* 51.3, 352, p. 352. arXiv: 1903.06844 [astro-ph.HE].

Carnall, A. C. et al. (July 2015). "Two bright z > 6 quasars from VST ATLAS and a new method of optical plus mid-infrared colour selection." In: *MNRAS* 451, pp. L16–L20. DOI: 10.1093/mnrasl/slv057. arXiv: 1502.07748 [astro-ph.GA].

Chon, Sunmyon et al. (Dec. 2016). "Cosmological Simulations of Early Black Hole Formation: Halo Mergers, Tidal Disruption, and the Conditions for Direct Collapse". In: *ApJ* 832.2, 134, p. 134. DOI: 10.3847/0004-637X/832/2/134. arXiv: 1603.08923 [astro-ph.GA].

Debuhr, Jackson, Eliot Quataert, and Chung-Pei Ma (Mar. 2012). "Galaxy-scale outflows driven by active galactic nuclei". In: *MNRAS* 420.3, pp. 2221–2231. DOI: 10.1111/j.1365-2966.2011.20187.x. arXiv: 1107.5579 [astro-ph.CO].

Devecchi, B. and M. Volonteri (Mar. 2009). "Formation of the First Nuclear Clusters and Massive Black Holes at High Redshift". In: *ApJ* 694.1, pp. 302–313. DOI: 10.1088/0004-637X/694/1/302. arXiv: 0810.1057 [astro-ph].

Dijkstra, Mark, Andrea Ferrara, and Andrei Mesinger (Aug. 2014). "Feedback-regulated supermassive black hole seed formation". In: *MNRAS* 442.3, pp. 2036–2047. DOI: 10.1093/mnras/stu1007. arXiv: 1405.6743 [astro-ph.GA].

Dubois, Yohan et al. (Sept. 2015). "Black hole evolution - I. Supernova-regulated black hole growth". In: *MNRAS* 452.2, pp. 1502–1518. DOI: 10.1093/mnras/stv1416. arXiv: 1504.00018 [astro-ph.GA].

Eggum, G. E., F. V. Coroniti, and J. I. Katz (Dec. 1987). "Radiation-Hydrodynamic Calculation of Sub-Eddington Accretion Disks". In: *ApJ* 323, p. 634. DOI: 10.1086/165859.

— (July 1988). "Radiation Hydrodynamic Calculation of Super-Eddington Accretion Disks". In: *APJ* 330, p. 142. DOI: 10.1086/166462.

Fan, Xiaohui et al. (Apr. 2003). "A Survey of z>5.7 Quasars in the Sloan Digital Sky Survey. II. Discovery of Three Additional Quasars at z>6". In: *AJ* 125.4, pp. 1649–1659. DOI: 10.1086/368246. arXiv: astro-ph/0301135 [astro-ph].

Ferrara, A. et al. (Sept. 2014). "Initial mass function of intermediate-mass black hole seeds". In: *MNRAS* 443.3, pp. 2410–2425. DOI: 10.1093/mnras/stu1280. arXiv: 1406.6685 [astro-ph.GA].

Fujita, Mitsutaka and Toru Okuda (Dec. 1998). "Two-Dimensional Accretion Disks at Subcritical Luminosity". In: *PASJ* 50, pp. 639–652. DOI: 10.1093/pasj/50.6.639.

Gaspari, M., M. Ruszkowski, and P. Sharma (Feb. 2012). "Cause and Effect of Feedback: Multiphase Gas in Cluster Cores Heated by AGN Jets". In: *ApJ* 746.1, 94, p. 94. DOI: 10.1088/0004-637X/746/1/94. arXiv: 1110.6063 [astro-ph.CO].

Graham, Alister W. (Jan. 2016). "Galaxy Bulges and Their Massive Black Holes: A Review". In: *Galactic Bulges*. Ed. by Eija Laurikainen, Reynier Peletier, and Dimitri Gadotti. Vol. 418. Astrophysics and Space Science Library, p. 263. DOI: 10.1007/978-3-319-19378-6_11. arXiv: 1501.02937 [astro-ph.GA].

Habouzit, Mélanie et al. (Apr. 2019). "Linking galaxy structural properties and star formation activity to black hole activity with IllustrisTNG". In: *MNRAS* 484.4, pp. 4413–4443. DOI: 10.1093/mnras/stz102. arXiv: 1809.05588 [astro-ph.GA].

Harrison, Fiona A. et al. (June 2013). "The Nuclear Spectroscopic Telescope Array (NuSTAR) High-energy X-Ray Mission". In: *ApJ* 770.2, 103, p. 103. DOI: 10.1088/0004-637X/770/2/103. arXiv: 1301.7307 [astro-ph.IM].

Hawley, Scott H. and Matthew W. Choptuik (Nov. 2000). "Boson stars driven to the brink of black hole formation". In: *Physical Review D* 62.10, 104024, p. 104024. DOI: 10.1103/PhysRevD.62.104024. arXiv: gr-qc/0007039 [gr-qc].

Hayashi, M. R., K. Shibata, and R. Matsumoto (Sept. 1996). "X-Ray Flares and Mass Outflows Driven by Magnetic Interaction between a Protostar and Its Surrounding Disk". In: *ApJ* 468, p. L37. DOI: 10.1086/310222. arXiv: astro-ph/9606157 [astro-ph].

Heger, A. et al. (July 2003). "How Massive Single Stars End Their Life". In: *ApJ* 591.1, pp. 288–300. DOI: 10.1086/375341. arXiv: astro-ph/0212469 [astro-ph].

Hirose, Shigenobu, Julian H. Krolik, and James M. Stone (Apr. 2006). "Vertical Structure of Gas Pressure-dominated Accretion Disks with Local Dissipation of Turbulence and Radiative Transport". In: *ApJ* 640.2, pp. 901–917. DOI: 10.1086/499153. arXiv: astro-ph/0510741 [astro-ph].

Ho, Luis C. Washington) (Jan. 2004). "Black Hole Demography from Nearby Active Galactic Nuclei". In: *Coevolution of Black Holes and Galaxies*. Ed. by Luis C. Ho, p. 292. arXiv: astro-ph/0401527 [astro-ph].

Hopkins, Philip F., Gordon T. Richards, and Lars Hernquist (Jan. 2007). "An Observational Determination of the Bolometric Quasar Luminosity Function". In: *ApJ* 654.2, pp. 731–753. DOI: 10.1086/509629. arXiv: astro-ph/0605678 [astro-ph].

Inayoshi, Kohei, Zoltán Haiman, and Jeremiah P. Ostriker (July 2016). "Hyper-Eddington accretion flows on to massive black holes". In: *MNRAS* 459.4, pp. 3738–3755. DOI: 10.1093/mnras/stw836. arXiv: 1511.02116 [astro-ph.HE].

Inayoshi, Kohei, Eli Visbal, and Zoltán Haiman (Aug. 2020). "The Assembly of the First Massive Black Holes". In: *ARA&A* 58, pp. 27–97. DOI: 10.1146/annurev-astro-120419-014455. arXiv: 1911.05791 [astro-ph.GA].

Jiang, Linhua et al. (Dec. 2016). "The Final SDSS High-redshift Quasar Sample of 52 Quasars at z>5.7". In: *ApJ* 833.2, 222, p. 222. DOI: 10.3847/1538-4357/833/2/222. arXiv: 1610.05369 [astro-ph.GA].

Jiang, Yan-Fei, James M. Stone, and Shane W. Davis (Dec. 2014). "A Global Three-dimensional Radiation Magneto-hydrodynamic Simulation of Super-Eddington Accretion Disks". In: *ApJ* 796.2, 106, p. 106. DOI: 10.1088/0004-637X/796/2/106. arXiv: 1410.0678 [astro-ph.HE].

— (Aug. 2019). "Super-Eddington Accretion Disks around Supermassive Black Holes". In: *ApJ* 880.2, 67, p. 67. DOI: 10.3847/1538-4357/ab29ff. arXiv: 1709.02845 [astro-ph.HE].

Kato, Nanako et al. (Oct. 2020). "Subaru High-z Exploration of Low-Luminosity Quasars (SHELLQs). IX. Identification of two red quasars at z > 5.6". In: *PASJ* 72.5, 84, p. 84. DOI: 10.1093/pasj/psaa074. arXiv: 2007.08685 [astro-ph.GA].

Kawashima, Tomohisa et al. (Aug. 2009). "New Spectral State of Supercritical Accretion Flow with Comptonizing Outflow". In: *PASJ* 61, p. 769. DOI: 10.1093/pasj/61.4.769. arXiv: 0904.4123 [astro-ph.HE].

King, A. R., J. E. Pringle, and J. A. Hofmann (Apr. 2008). "The evolution of black hole mass and spin in active galactic nuclei". In: *MNRAS* 385.3, pp. 1621–1627. DOI: 10.1111/j.1365-2966.2008.12943.x. arXiv: 0801.1564 [astro-ph].

Kitaki, Takaaki et al. (Dec. 2017). "Theoretical modeling of Comptonized X-ray spectra of super-Eddington accretion flow: Origin of hard excess in ultraluminous X-ray sources". In: *PASJ* 69.6, 92, p. 92. DOI: 10.1093/pasj/psx101. arXiv: 1709.01531 [astro-ph.HE].

— (Jan. 2021). "Outflow from super-Eddington flow: where it originates from and how much impact it gives?" In: *arXiv e-prints*, arXiv:2101.11028, arXiv:2101.11028. DOI: 10.1093/pasj/psab011. arXiv: 2101.11028 [astro-ph.HE].

Kley, W. (Sept. 1989). "Radiation hydrodynamics of the boundary layer in accretion disks. II.Optically thick models." In: *A&A* 222, pp. 141–149.

Kley, W. and D. N. C. Lin (June 1999). "Evolution of FU Orionis Outbursts in Protostellar Disks". In: *ApJ* 518.2, pp. 833–847. DOI: 10.1086/307296.

Konoplya, R. A., J. Kunz, and A. Zhidenko (Feb. 2021). "Blandford-Znajek mechanism in the general axially-symmetric black-hole spacetime". In: *arXiv e-prints*, arXiv:2102.10649, arXiv:2102.10649. arXiv: 2102.10649 [gr-qc].

Kormendy, John and Luis C. Ho (Aug. 2013). "Coevolution (Or Not) of Supermassive Black Holes and Host Galaxies". In: *ARA&A* 51.1, pp. 511–653. DOI: 10.1146/annurev-astro-082708-101811. arXiv: 1304.7762 [astro-ph.CO].

Levermore, C. D. and G. C. Pomraning (Aug. 1981). "A flux-limited diffusion theory". In: *ApJ* 248, pp. 321–334. DOI: 10.1086/159157.

Loeb, Abraham and Frederic A. Rasio (Sept. 1994). "Collapse of Primordial Gas Clouds and the Formation of Quasar Black Holes". In: *ApJ* 432, p. 52. DOI: 10.1086/174548. arXiv: astro-ph/9401026 [astro-ph].

Machida, Mami and Ryoji Matsumoto (Sept. 2000). "Three-Dimensional Magnetohydrodynamical Accretion Flows into Black Holes". In: *arXiv e-prints*, astro-ph/0009004, astro–ph/0009004. arXiv: astro-ph/0009004 [astro-ph].

Madau, Piero and Martin J. Rees (Apr. 2001). "Massive Black Holes as Population III Remnants". In: *ApJ* 551.1, pp. L27–L30. DOI: 10.1086/319848. arXiv: astro-ph/0101223 [astro-ph].

Mathews, William G. and Fabrizio Brighenti (Jan. 2003). "Hot Gas in and around Elliptical Galaxies". In: *ARA&A* 41, pp. 191–239. DOI: 10.1146/annurev.astro.41.090401.094542. arXiv: astro-ph/0309553 [astro-ph].

Matsumoto, R. (Jan. 1999). "Three-dimensional Global MHD Simulations of Accretion Disks Advection Viscosity, and Fluctuations". In: *Disk Instabilities in Close Binary Systems*. Ed. by S. Mineshige and J. C. Wheeler, p. 303.

Matsuoka, Yoshiki et al. (Sept. 2016). "Subaru High-z Exploration of Low-luminosity Quasars (SHELLQs). I. Discovery of 15 Quasars and Bright Galaxies at 5.7 < z < 6.9". In: *ApJ* 828.1, 26, p. 26. DOI: 10.3847/0004-637X/828/1/26. arXiv: 1603.02281 [astro-ph.GA].

Matsuoka, Yoshiki et al. (Jan. 2018). "Subaru High-z Exploration of Low-Luminosity Quasars (SHELLQs). II. Discovery of 32 quasars and luminous galaxies at 5.7 < z $\leq$ 6.8". In: *PASJ* 70, S35, S35. DOI: 10.1093/pasj/psx046. arXiv: 1704.05854 [astro-ph.GA].

Matsuoka, Yoshiki et al. (Oct. 2019). "Subaru High-z Exploration of Low-luminosity Quasars (SHELLQs). X. Discovery of 35 Quasars and Luminous Galaxies at 5.7 $\leq$ z $\leq$ 7.0". In: *ApJ* 883.2, 183, p. 183. DOI: 10.3847/1538-4357/ab3c60. arXiv: 1908.07910 [astro-ph.GA].

Mazzucchelli, C. et al. (Nov. 2017). "Physical Properties of 15 Quasars at z $\gtrsim$ 6.5". In: *ApJ* 849.2, 91, p. 91. DOI: 10.3847/1538-4357/aa9185. arXiv: 1710.01251 [astro-ph.GA].

McKinney, Jonathan C. et al. (July 2014). "Three-dimensional general relativistic radiation magnetohydrodynamical simulation of super-Eddington accretion, using a new code HARMRAD with M1 closure". In: *MNRAS* 441.4, pp. 3177–3208. DOI: 10.1093/mnras/stu762. arXiv: 1312.6127 [astro-ph.CO].

Merloni, Andrea and Sebastian Heinz (2013). "Evolution of Active Galactic Nuclei". In: *Planets, Stars and Stellar Systems. Volume 6: Extragalactic Astronomy and Cosmology*. Ed. by Terry D. Oswalt and William C. Keel. Vol. 6, p. 503. DOI: 10.1007/978-94-007-5609-0_11.

Narayan, Ramesh, Aleksander Sądowski, and Roberto Soria (Aug. 2017). "Spectra of black hole accretion models of ultraluminous X-ray sources". In: *MNRAS* 469.3, pp. 2997–3014. DOI: 10.1093/mnras/stx1027. arXiv: 1702.01158 [astro-ph.HE].

Natarajan, Priyamvada (Mar. 2011). "The formation and evolution of massive black hole seeds in the early Universe". In: *Bulletin of the Astronomical Society of India* 39, pp. 145–161. arXiv: 1104.4797 [astro-ph.CO].

Nomura, Mariko et al. (Feb. 2016). "Radiation hydrodynamic simulations of line-driven disk winds for ultra-fast outflows". In: *PASJ* 68.1, 16, p. 16. DOI: 10.1093/pasj/psv124. arXiv: 1511.08815 [astro-ph.HE].

Ohsuga, Ken and Shin Mineshige (July 2011). "Global Structure of Three Distinct Accretion Flows and Outflows around Black Holes from Two-dimensional Radiation-magnetohydrodynamic Simulations". In: *ApJ* 736.1, 2, p. 2. DOI: 10.1088/0004-637X/736/1/2. arXiv: 1105.5474 [astro-ph.HE].

Ohsuga, Ken et al. (July 2005). "Supercritical Accretion Flows around Black Holes: Two-dimensional, Radiation Pressure-dominated Disks with Photon Trapping". In: *ApJ* 628.1, pp. 368–381. DOI: 10.1086/430728. arXiv: astro-ph/0504168 [astro-ph].

Ohsuga, Ken et al. (June 2009). "Global Radiation-Magnetohydrodynamic Simulations of Black-Hole Accretion Flow and Outflow: Unified Model of Three States". In: *PASJ* 61.3, pp. L7–L11. DOI: 10.1093/pasj/61.3.L7. arXiv: 0903.5364 [astro-ph.HE].

Okuda, Toru and Mitsutaka Fujita (Apr. 2000). "Super-Eddington Accretion-Disk Models for SS 433". In: *PASJ* 52, p. L5. DOI: 10.1093/pasj/52.2.L5.

Okuda, Toru, Mitsutaka Fujita, and Shiro Sakashita (Dec. 1997). "Two-Dimensional Accretion Disk Models: Inner Accretion Disks of FU Orionis Objects". In: *PASJ* 49, pp. 679–697. DOI: 10.1093/pasj/49.6.679.

Onoue, Masafusa et al. (Aug. 2019). "Subaru High-z Exploration of Low-luminosity Quasars (SHELLQs). VI. Black Hole Mass Measurements of Six Quasars at 6.1 $\leq$ z $\leq$ 6.7". In: *ApJ* 880.2, 77, p. 77. DOI: 10.3847/1538-4357/ab29e9. arXiv: 1904.07278 [astro-ph.GA].

Pacucci, Fabio, Marta Volonteri, and Andrea Ferrara (Sept. 2015). "The growth efficiency of high-redshift black holes". In: *MNRAS* 452.2, pp. 1922–1933. DOI: 10.1093/mnras/stv1465. arXiv: 1506.04750 [astro-ph.GA].

Paczyński, B. and P. J. Wiita (Aug. 1980). "Thick accretion disks and supercritical luminosities." In: *A&A* 500, pp. 203–211.

Paliya, Vaidehi S. et al. (Mar. 2019). "Supermassive black holes at high redshifts". In: *arXiv e-prints*, arXiv:1903.06106, arXiv:1903.06106. arXiv: 1903.06106 [astro-ph.HE].

Pillepich, Annalisa et al. (Jan. 2018). "Simulating galaxy formation with the IllustrisTNG model". In: *MNRAS* 473.3, pp. 4077–4106. DOI: 10.1093/mnras/stx2656. arXiv: 1703.02970 [astro-ph.GA].

Portegies Zwart, Simon F. and Stephen L. W. McMillan (Sept. 2002). "The Runaway Growth of Intermediate-Mass Black Holes in Dense Star Clusters". In: *ApJ* 576.2, pp. 899–907. DOI: 10.1086/341798. arXiv: astro-ph/0201055 [astro-ph].

Portegies Zwart, Simon F. et al. (Apr. 2004). "Formation of massive black holes through runaway collisions in dense young star clusters". In: *Nature* 428.6984, pp. 724–726. DOI: 10.1038/nature02448. arXiv: astro-ph/0402622 [astro-ph].

Reed, S. L. et al. (July 2017). "Eight new luminous z $\geq$ 6 quasars discovered via SED model fitting of VISTA, WISE and Dark Energy Survey Year 1 observations". In: *MNRAS* 468.4, pp. 4702–4718. DOI: 10.1093/mnras/stx728. arXiv: 1701.04852 [astro-ph.GA].

Reed, S. L. et al. (Aug. 2019). "Three new VHS-DES quasars at 6.7 < z < 6.9 and emission line properties at z > 6.5". In: *MNRAS* 487.2, pp. 1874–1885. DOI: 10.1093/mnras/stz1341. arXiv: 1901.07456 [astro-ph.GA].

Rees, Martin J. (Jan. 1984). "Black Hole Models for Active Galactic Nuclei". In: *Annual Review of Astron and Astrophys* 22, pp. 471–506. DOI: 10.1146/annurev.aa.22.090184.002351.

Regan, John A. and Martin G. Haehnelt (June 2009). "Pathways to massive black holes and compact star clusters in pre-galactic dark matter haloes with virial temperatures >$\sim$10000K". In: *MNRAS* 396.1, pp. 343–353. DOI: 10.1111/j.1365-2966.2009.14579.x. arXiv: 0810.2802 [astro-ph].

Ressler, S. M., E. Quataert, and J. M. Stone (Mar. 2020). "The surprisingly small impact of magnetic fields on the inner accretion flow of Sagittarius A* fueled by stellar winds". In: *MNRAS* 492.3, pp. 3272–3293. DOI: 10.1093/mnras/stz3605. arXiv: 2001.04469 [astro-ph.HE].

Richard-Laferrière, A. et al. (Dec. 2020). "On the relation between mini-halos and AGN feedback in clusters of galaxies". In: *MNRAS* 499.2, pp. 2934–2958. DOI: 10.1093/mnras/staa2877. arXiv: 2007.01306 [astro-ph.GA].

Ross, Nicholas P. and Nicholas J. G. Cross (May 2020). "The near and mid-infrared photometric properties of known redshift z $\geq$ 5 quasars". In: *MNRAS* 494.1, pp. 789–803. DOI: 10.1093/mnras/staa544. arXiv: 1906.06974 [astro-ph.GA].

Ruszkowski, Mateusz et al. (May 2019). "Supermassive Black Hole Feedback". In: *BAAS* 51.3, 326, p. 326. arXiv: 1903.09686 [astro-ph.HE].

Rybicki, George B. and Alan P. Lightman (1986). *Radiative Processes in Astrophysics*.

Sakurai, Yuya, Kohei Inayoshi, and Zoltán Haiman (Oct. 2016). "Hyper-Eddington mass accretion on to a black hole with super-Eddington luminosity". In: *MNRAS* 461.4, pp. 4496–4504. DOI: 10.1093/mnras/stw1652. arXiv: 1605.09105 [astro-ph.HE].

Shakura, N. I. and R. A. Sunyaev (June 1973). "Reprint of 1973A&A....24..337S. Black holes in binary systems. Observational appearance." In: *A&A* 500, pp. 33–51.

Shlosman, Isaac et al. (Feb. 2016). "Supermassive black hole seed formation at high redshifts: long-term evolution of the direct collapse". In: *MNRAS* 456.1, pp. 500–511. DOI: 10.1093/mnras/stv2700. arXiv: 1508.05098 [astro-ph.GA].

Sądowski, Aleksander and Ramesh Narayan (Mar. 2016). "Three-dimensional simulations of supercritical black hole accretion discs - luminosities, photon trapping and variability". In: *MNRAS* 456.4, pp. 3929–3947. DOI: 10.1093/mnras/stv2941. arXiv: 1509.03168 [astro-ph.HE].

Sądowski, Aleksander et al. (Feb. 2015). "Global simulations of axisymmetric radiative black hole accretion discs in general relativity with a mean-field magnetic dynamo". In: *MNRAS* 447.1, pp. 49–71. DOI: 10.1093/mnras/stu2387. arXiv: 1407.4421 [astro-ph.HE].

Stone, James M., James E. Pringle, and Mitchell C. Begelman (Dec. 1999). "Hydrodynamical non-radiative accretion flows in two dimensions". In: *MNRAS* 310.4, pp. 1002–1016. DOI: 10.1046/j.1365-8711.1999.03024.x. arXiv: astro-ph/9908185 [astro-ph].

Takahashi, Hiroyuki R. et al. (July 2016). "Formation of Overheated Regions and Truncated Disks around Black Holes: Three-dimensional General Relativistic Radiation-magnetohydrodynamics Simulations". In: *ApJ* 826.1, 23, p. 23. DOI: 10.3847/0004-637X/826/1/23. arXiv: 1605.04992 [astro-ph.GA].

Takeo, Eishun, Kohei Inayoshi, and Shin Mineshige (Sept. 2020). "Hyper-Eddington accretion flows on to black holes accompanied by powerful outflows". In: *MNRAS* 497.1, pp. 302–317. DOI: 10.1093/mnras/staa1906. arXiv: 2002.07187 [astro-ph.HE].

Takeo, Eishun et al. (May 2018). "Rapid growth of black holes accompanied with hot or warm outflows exposed to anisotropic super-Eddington radiation". In: *MNRAS* 476.1, pp. 673–682. DOI: 10.1093/mnras/sty264. arXiv: 1705.05382 [astro-ph.HE].

— (Sept. 2019). "Super-Eddington growth of black holes in the early universe: effects of disc radiation spectra". In: *MNRAS* 488.2, pp. 2689–2700. DOI: 10.1093/mnras/stz1899. arXiv: 1901.04514 [astro-ph.HE].

Tremmel, M. et al. (Mar. 2019). "Introducing ROMULUSC: a cosmological simulation of a galaxy cluster with an unprecedented resolution". In: *MNRAS* 483.3, pp. 3336–3362. DOI: 10.1093/mnras/sty3336. arXiv: 1806.01282 [astro-ph.GA].

Turner, N. J. and J. M. Stone (July 2001). "A Module for Radiation Hydrodynamic Calculations with ZEUS-2D Using Flux-limited Diffusion". In: *ApJs* 135.1, pp. 95–107. DOI: 10.1086/321779. arXiv: astro-ph/0102145 [astro-ph].

Turner, N. J. et al. (Aug. 2003). "Local Three-dimensional Simulations of Magnetorotational Instability in Radiation-dominated Accretion Disks". In: *ApJ* 593.2, pp. 992–1006. DOI: 10.1086/376615. arXiv: astro-ph/0304511 [astro-ph].

Valiante, Rosa et al. (July 2017). "On the Formation of the First Quasars". In: *PASA* 34, e031, e031. DOI: 10.1017/pasa.2017.25. arXiv: 1703.03808 [astro-ph.GA].

Vito, F. et al. (Oct. 2019). "The X-ray properties of z > 6 quasars: no evident evolution of accretion physics in the first Gyr of the Universe". In: *A&A* 630, A118, A118. DOI: 10.1051/0004-6361/201936217. arXiv: 1908.09849 [astro-ph.GA].

Vogelsberger, Mark et al. (Apr. 2019). "Evaporating the Milky Way halo and its satellites with inelastic self-interacting dark matter". In: *MNRAS* 484.4, pp. 5437–5452. DOI: 10.1093/mnras/stz340. arXiv: 1805.03203 [astro-ph.GA].

Volonteri, Marta (July 2010). "Formation of supermassive black holes". In: *A&AR* 18.3, pp. 279–315. DOI: 10.1007/s00159-010-0029-x. arXiv: 1003.4404 [astro-ph.CO].

Volonteri, Marta and Mitchell C. Begelman (Dec. 2010). "Quasi-stars and the cosmic evolution of massive black holes". In: *MNRAS* 409.3, pp. 1022–1032. DOI: 10.1111/j.1365-2966.2010.17359.x. arXiv: 1003.5220 [astro-ph.HE].

Wang, Feige et al. (Mar. 2016). "A Survey of Luminous High-redshift Quasars with SDSS and WISE. I. Target Selection and Optical Spectroscopy". In: *ApJ* 819.1, 24, p. 24. DOI: 10.3847/0004-637X/819/1/24. arXiv: 1602.04659 [astro-ph.GA].

Wang, Feige et al. (Oct. 2019). "Exploring Reionization-era Quasars. III. Discovery of 16 Quasars at $6.4 \lesssim z \lesssim 6.9$ with DESI Legacy Imaging Surveys and the UKIRT Hemisphere Survey and Quasar Luminosity Function at $z \sim 6.7$". In: *ApJ* 884.1, 30, p. 30. DOI: 10.3847/1538-4357/ab2be5. arXiv: 1810.11926 [astro-ph.GA].

Watarai, Ken-ya, Tsunefumi Mizuno, and Shin Mineshige (Mar. 2001). "Slim-Disk Model for Ultraluminous X-Ray Sources". In: *ApJL* 549.1, pp. L77–L80. DOI: 10.1086/319125. arXiv: astro-ph/0011434 [astro-ph].

Willott, Chris J. et al. (Mar. 2010). "The Canada-France High-z Quasar Survey: Nine New Quasars and the Luminosity Function at Redshift 6". In: *AJ* 139.3, pp. 906–918. DOI: 10.1088/0004-6256/139/3/906. arXiv: 0912.0281 [astro-ph.CO].

Wise, John H. et al. (Jan. 2019). "Formation of massive black holes in rapidly growing pre-galactic gas clouds". In: *Nature* 566.7742, pp. 85–88. DOI: 10.1038/s41586-019-0873-4. arXiv: 1901.07563 [astro-ph.GA].

Yang, Jinyi et al. (Oct. 2018). "Filling in the Quasar Redshift Gap at $z \sim 5.5$ II: A Complete Survey of Luminous Quasars in the Post-Reionization Universe". In: *arXiv e-prints*, arXiv:1810.11927, arXiv:1810.11927. arXiv: 1810.11927 [astro-ph.GA].

Yang, Jinyi et al. (July 2020). "Pōniuā'ena: A Luminous z = 7.5 Quasar Hosting a 1.5 Billion Solar Mass Black Hole". In: *ApJ* 897.1, L14, p. L14. DOI: 10.3847/2041-8213/ab9c26. arXiv: 2006.13452 [astro-ph.GA].

Yuan, Feng, Maochun Wu, and Defu Bu (Dec. 2012). "Numerical Simulation of Hot Accretion Flows. I. A Large Radial Dynamical Range and the Density Profile of Accretion Flow". In: *ApJ* 761.2, 129, p. 129. DOI: 10.1088/0004-637X/761/2/129. arXiv: 1206.4157 [astro-ph.HE].